

# The traveling-PWN modeling attempt on the mysterious LHAASO dumbbell-like structure

Caijin Xie<sup>1</sup>, Yihan Liu<sup>1</sup>, Chengyu Shao<sup>1</sup>, Yudong Cui<sup>1,\*</sup>, and Lili Yang<sup>1,2,\*\*</sup>

<sup>1</sup> School of Physics and Astronomy, Sun Yat-Sen University, No. 2 Daxue Road, 519082, Zhuhai China

<sup>2</sup> Centre for Astro-Particle Physics, University of Johannesburg, P.O. Box 524, Auckland Park 2006, South Africa

October 15, 2024

## ABSTRACT

*Context.* The first LHAASO catalog presents six mysterious Ultra-High-Energy (UHE)  $\gamma$ -ray sources – 1LHAASO J0007+5659u, 1LHAASO J0206+4302u, 1LHAASO J0212+4254u, 1LHAASO J0216+4237u, 1LHAASO J1740+0948u and 1LHAASO J1959+1129u, which only have  $> 25$  TeV emission detected. No counterparts of the six sources have been observed, except two pulsars PSR J0218+4232 and PSR J1740+1000. Three of them – 1LHAASO J0206+4302u, 1LHAASO J0212+4254u and 1LHAASO J0216+4237u are connected on the significance map and constituted a dumbbell-like structure. They are close in position and show a similar spectral shape, suggesting a physical association among them.

*Aims.* To explain the origin of the six LHAASO sources, especially the interesting dumbbell-like structure, we conducted the leptonic and hadronic modeling research on them according to our multi-wavelength and multi-messenger study. For the dumbbell-like structure, a traveling Pulsar Wind Nebula (PWN) model is considered.

*Methods.* The multi-wavelength and multi-messenger study is based on the Fermi-LAT, Swift-XRT, Planck, LAMBDA and Ice-Cube neutrino datasets. In the traveling-PWN modeling research, we assume an isotropic and homogeneous diffusion condition and discussed the influence of diffusion coefficient, distance and proper-motion velocity.

*Results.* No counterparts are discovered in our multi-wavelength and multi-messenger study, except the two known pulsars. The traveling-PWN modeling attempt with a single traveling-PWN seems to be difficult to explain the dumbbell-like structure, unless the diffusion coefficient is extremely low and the pulsar has a proper-motion velocity over  $1200 \text{ km s}^{-1}$ . We also explore the double traveling-PWNe explanation and find the occurring possibilities of these two explanations are much lower than that of an ordinary triple PWNe explanation. Moreover, according to our model, the only known pulsar nearby – PSR J0218+4232 is unlikely to be associated with the dumbbell-like structure in an isotropic and homogeneous diffusion environment. The TeV emission of this pulsar is far from explaining even the eastern part of the structure.

**Key words.** LHAASO UHE sources – Traveling-PWN modeling

## 1. Introduction

As one of the state-of-the-art Cosmic Ray (CR) and  $\gamma$ -ray observatory, the Large High Altitude Air Shower Observatory (LHAASO) experiment located at 4410 m above sea level in Daocheng site, Sichuan province, has an excellent detection ability at Ultra-High-Energy (UHE) band and can expand the way for discovering new UHE  $\gamma$ -ray sources. LHAASO covers the energies from 100 GeV to 1 EeV (Di Sciacio et al. 2016) and achieves sensitivity below  $1 \times 10^{-12} \text{ erg cm}^{-2} \text{ s}^{-1} \text{ sr}^{-1}$  at TeV energy (Neronov & Semikoz 2020). It consists of three major parts – Water Cherenkov Detector Array (WCDA) for TeV  $\gamma$ -ray detection, Kilometer Squared Array (KM2A) for detecting  $\gamma$ -ray above 10 TeV and a Wide Field-of-view Cherenkov/fluorescence Telescope Array (WFCTA) mainly for CR detection (Cao et al. 2024). Recently, the LHAASO collaboration have presented its first catalog of  $\gamma$ -ray sources, which reports 10 sources without 1~25 TeV  $\gamma$  photons detected by WCDA, but have emissions ranging from 25 TeV to over 100 TeV observed by KM2A (Cao et al. 2024). To avoid the complex background, our work focus on the six lonely  $> 25$  TeV sources located outside the Galactic plane, which are 1LHAASO J0007+5659u, 1LHAASO

J0206+4302u, 1LHAASO J0212+4254u, 1LHAASO J0216+4237u, 1LHAASO J1740+0948u and 1LHAASO J1959+1129u. So far, only two pulsars – PSR J0218+4232 and PSR J1740+1000 are found close to them. If these lonely  $> 25$  TeV sources are Geminga-like Pulsar Wind Nebula (PWN) halos, their electron cutoff energies will be far beyond 100 TeV. A more interesting thing is that the sources 1LHAASO J0206+4302u, 1LHAASO J0212+4254u and 1LHAASO J0216+4237u are spatially connected (forming an extended structure like a dumbbell on the significance map) and share a similar spectral shape (spectral index  $\approx 2.5$ ). This motivates us to explore the possible origins of them, which could imply some new physical mechanisms.

The six LHAASO UHE sources mentioned above are all point-like sources that only detected by KM2A (Cao et al. 2024). The experimental data were fitted by a power-law function as the fixed reference energy was 50 TeV (Cao et al. 2024). The 1LHAASO J0007+5659u (J0007+5659u for short in the remaining text) has a Test Statistic (TS) value of 43.6 at energies over 100 TeV, and its spectral index is  $3.10 \pm 0.20$  (Cao et al. 2024). The galactic longitude and latitude of J0007+5659u are  $116.94^\circ$  and  $-5.36^\circ$ , respectively. The spatially associated sources 1LHAASO J0206+4302u, 1LHAASO J0212+4254u and 1LHAASO J0216+4237u (J0206+4302u, J0212+4254u and

\* cuiyd@mail.sysu.edu.cn

\*\* yanglli5@mail.sysu.edu.cn

**Table 1.** Information about the six UHE  $\gamma$ -ray sources only detected by LHAASO-KM2A

Source	Galactic longitude (deg)	Galactic latitude (deg)	TS <sub>100</sub> <sup>a</sup>	Spectral index	Nearby pulsars
J0007+5659u	116.94	-5.36	43.6	3.10	/
J0206+4302u	137.27	-17.71	82.8	2.62	/
J0212+4254u	138.28	-17.55	30.2	2.45	/
J0216+4237u	139.17	-17.55	65.6	2.58	PSR J0218+4232
J1740+0948u	33.79	20.26	37.2	3.13	PSR J1740+1000
J1959+1129u	51.10	-9.42	60.8	2.69	/

**Notes.** <sup>a</sup>TS value at energies over 100 TeV.

J0216+4237u for short in the remaining text) have TS value of 82.8, 30.2 and 65.6 at energies over 100 TeV, and their spectral index are  $2.62 \pm 0.16$ ,  $2.45 \pm 0.23$  and  $2.58 \pm 0.17$  (Cao et al. 2024). The galactic longitudes of these three sources are  $137.27^\circ$ ,  $138.28^\circ$  and  $139.17^\circ$  while their galactic latitudes are  $-17.71^\circ$ ,  $-17.55^\circ$  and  $-17.55^\circ$ , respectively. There is an energetic millisecond pulsar, PSR J0218+4232, located at that sky region. However, no physical associations among these three sources and the pulsar can be confirmed, due to the large position offset (Cao et al. 2024) and the low TeV emission predicted by the observation of Fermi Large Area Telescope (Fermi-LAT) and Major Atmospheric Gamma Imaging Cherenkov (MAGIC) (Acciari et al. 2021). The 1LHAASO J1740+0948u (J1740+0948u for short in the remaining text) has a TS value of 37.2 at energies over 100 TeV and its spectral index is  $3.13 \pm 0.15$  (Cao et al. 2024). J1740+0948u locate far away from Galactic plane with galactic longitude of  $33.79^\circ$  and galactic latitude of  $20.26^\circ$ . A middle-aged radio pulsar PSR J1740+1000 is close to it, and the position offset is about  $0.2^\circ$ . Due to the lack of observation, the physical association between J1740+0948u and PSR J1740+1000 is still in mystery. At last, the 1LHAASO J1959+1129u (J1959+1129u for short in remaining text) with spectral index of  $2.69 \pm 0.17$  has a TS value of 60.8 at energies over 100 TeV (Cao et al. 2024). Its galactic longitude and latitude are  $51.1^\circ$  and  $-9.42^\circ$ , respectively. As a brief summary, we present the position and spectral information about the six sources in Table 1.

For the attractive dumbbell-like structure consisting of J0206+4302u, J0212+4254u and J0216+4237u, we attempt to use the proper-motion of the central pulsar of PWN to explain its origin and study the traveling-PWN model under the isotropic and homogeneous diffusion condition. A previous work has discussed the impact of pulsar proper-motion on the morphology of its  $\gamma$ -ray halo (Zhang et al. 2021). The results infer that it is difficult to use the proper-motion of a middle-aged pulsar with common distance and proper-motion velocity to explain an extended structure. However, we think it is necessary to explore the model containing a single traveling-PWN within a broader parameter space and study the model with multiple traveling-PWNe involved as well as the exact occurring possibilities of different scenarios.

In this work, to explore the origin of these LHAASO sources, we firstly conduct a multi-wavelength and multi-messenger study, aiming to check if there are any possible counterparts of them discovered at other energy bands. The results are presented in Section 2 and some details about data analysis are provided in Section A of Appendix. Based on the constraints set by the multi-wavelength and multi-messenger study, we perform the leptonic and hadronic modeling research on the six sources. The best-fit models are presented in Section 3. The expected neutrino flux in the hadronic scenario compared with the sensitivity

of next generation neutrino observatory is shown in Section B of Appendix. As mentioned before, the traveling-PWN modeling attempt under the isotropic and homogeneous diffusion environment for explaining the interesting dumbbell-like structure is discussed in Section 4. We have explored the influence of diffusion coefficient, distance and proper-motion velocity on the final morphology of  $\gamma$ -ray halo. With appropriate parameters applied, the models containing one traveling-PWN, two traveling-PWNe and three PWNe (equals to the number of UHE sources recognized by LHAASO) as well as their occurring possibilities in the LHAASO sky are also studied. Finally, the conclusion and discussion are given in Section 5.

## 2. Multi-wavelength and multi-messenger study

### 2.1. Fermi-LAT dataset

Fermi-LAT was placed into orbit at 2008 June 11. It is an all-sky  $\gamma$ -ray spatial observatory covering energies from 20 MeV to over 300 GeV (Abdo et al. 2009), with a typical sensitivity of  $\sim 10^{-12}$  erg cm<sup>-2</sup> s<sup>-1</sup> for observation of 10 years (Funk et al. 2013). To investigate the morphology of the six LHAASO UHE sources at lower energy band, we analyzed 10 years of data recorded by Fermi-LAT from 2014 January 1 to 2024 January 1 with energies ranging from 300 MeV to 300 GeV. As a result, at the exact spots of the six LHAASO sources, no abundant observation data were obtained and the  $\gamma$ -ray fluxes of the six sources acquired by maximum-likelihood analysis had error bars larger than truth-values. The analysis were conducted by using the publicly available toolkit **Fermitools**. Since no accurate  $\gamma$ -ray fluxes of the six sources could be extracted from Fermi-LAT dataset, the upper limits of Spectral Energy Distribution (SED) were calculated and used to constrain the modeling research discussed in Section 3.

We also calculated the TS maps of the six LHAASO sources via **gttmap** function, to examine the  $\gamma$ -ray sources observed by Fermi-LAT. Fig. 1 (a)-(d) presents the TS map including all the fourth Fermi Large Area Telescope (4FGL) (Abdollahi et al. 2020) sources close to the six LHAASO sources (position offset  $< 0.5^\circ$ ). There are two 4FGL sources found within the  $0.5^\circ$  radius region centered on each LHAASO source and can be confirmed as the two known pulsars (PSR J0218+4232 and PSR J1740+1000) mentioned before<sup>1</sup>. Fig. 1 (e)-(h) shows the residual TS map with all 4FGL sources excluded, which suggest there are no other significant sources might be associated with the six LHAASO sources in the energy range of 300 MeV to 300 GeV. The details about the maximum-likelihood analysis and TS map calculation can be found in Subsection A.1 of Appendix.

<sup>1</sup> see in the Public List of LAT-Detected Gamma-Ray Pulsars on <https://confluence.slac.stanford.edu/display/GLAMCOG/Public+List+of+LAT-Detected+Gamma-Ray+Pulsars>

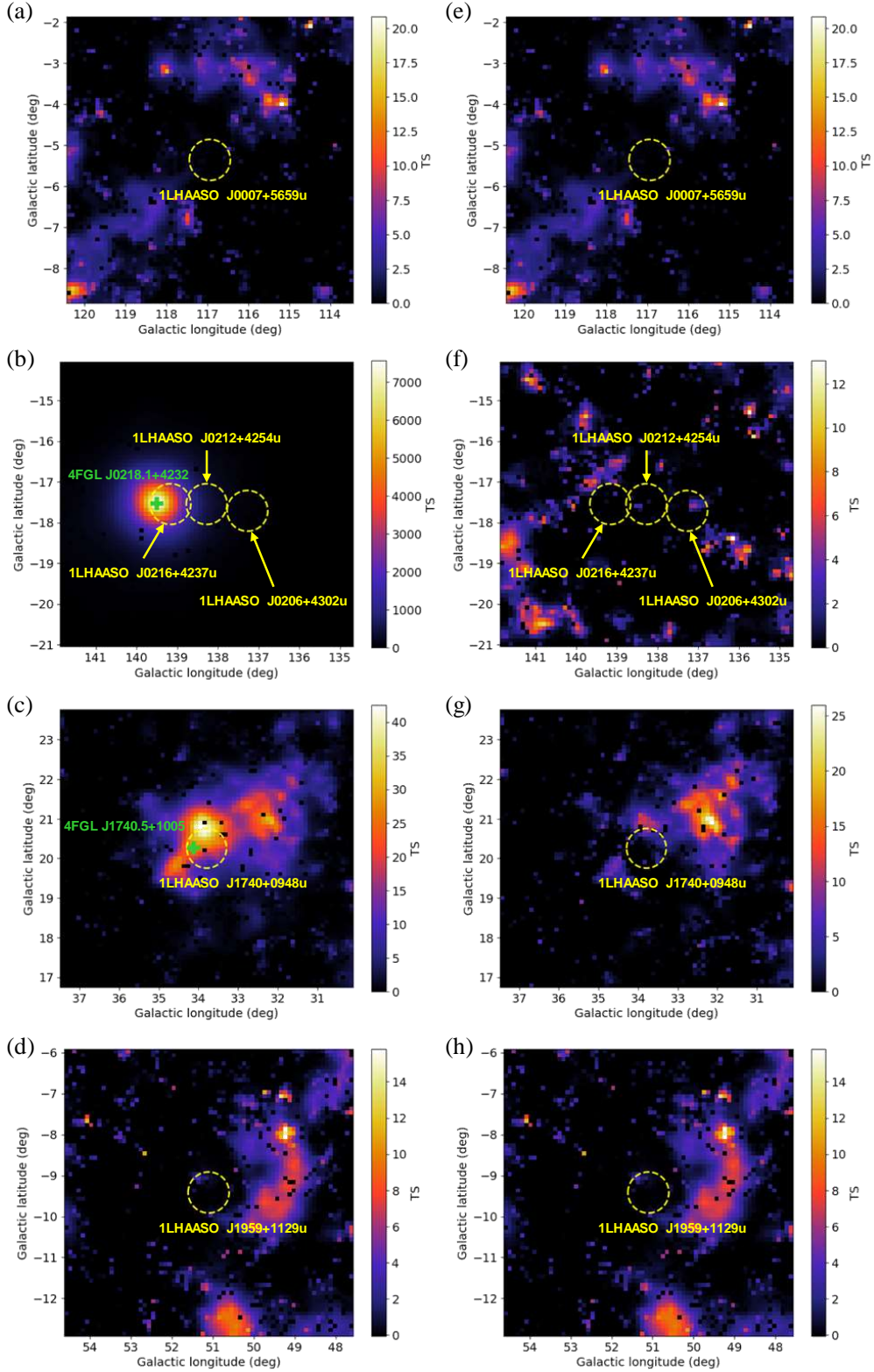


**Fig. 1.** Fermi TS maps within  $5^\circ$  radius Regions of Interest (ROIs) of the six LHAASO UHE sources. (a)-(d) TS maps with the 4FGL sources which are close to LHAASO sources remained. The reserved 4FGL sources are pointed out by green cross shapes. Yellow dashed circles of  $0.5^\circ$  radius centered on labeled LHAASO sources indicate the sky regions for filtering the 4FGL sources by position. (e)-(h) Residual maps with all 4FGL sources excluded.

## 2.2. Swift-XRT dataset

The Swift Gamma-Ray Explorer is a spatial observatory designed to make prompt multi-wavelength observations of

Gamma-Ray Bursts (GRBs) and GRB afterglows. The X-ray telescope integrated on the Swift satellite (Swift-XRT) enables it to precisely locate the positions of GRBs with a few arcseconds accuracy within 100 s of the burst onset (Burrows et al.

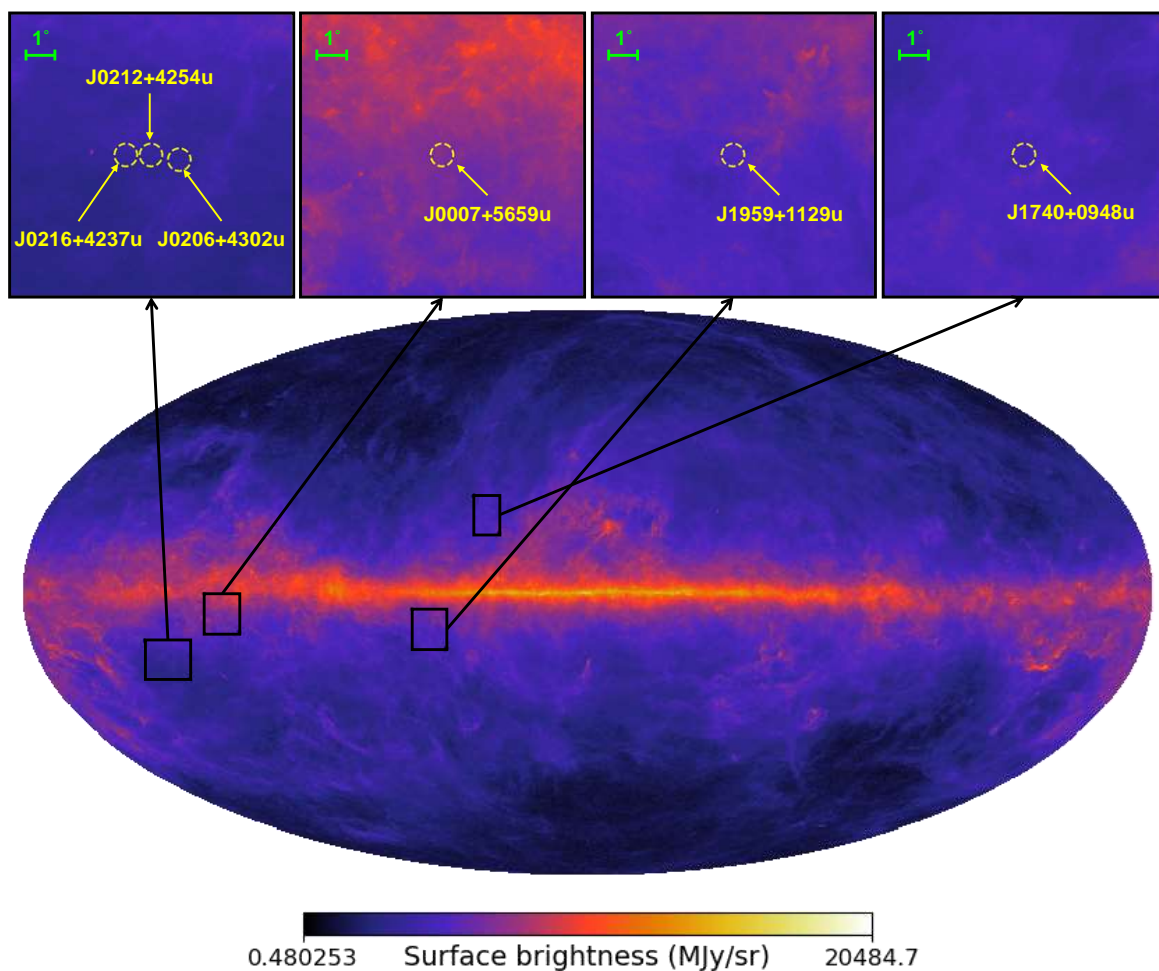


**Fig. 2.** Planck all-sky map at 857 GHz. The map is presented in Galactic coordinate system and the color-bar is plotted in logarithmic scale. The zoomed-in views of  $10^\circ \times 10^\circ$  ROIs centered on the six sources are presented at the top of the figure. The yellow dashed circles indicates the positions of labeled sources.

2005). The Swift-XRT covers the energy range from 0.2 keV to 10 keV, and its sensitivity is  $2 \times 10^{-14}$  erg cm $^{-2}$  s $^{-1}$  in  $10^4$  s (Burrows et al. 2005). We have searched for X-ray sources located approximate to the positions of the six LHAASO UHE sources (position offset  $< 0.3^\circ$ ) within the Swift-XRT dataset. As a result, no such sources were observed<sup>2</sup>. Moreover, among the six sources, the Swift-XRT only has X-ray data within the  $0.3^\circ$  radius ROI centered on J0206+4302u<sup>3</sup>. These data with exposure time of 1577.1 s were used to set constraint on SEDs of the six sources in keV band as no abundant efficient photons were detected. The results of upper limits were  $7.0 \times 10^{-14}$  erg cm $^{-2}$  s $^{-1}$  at 1.5 keV and  $6.1 \times 10^{-13}$  erg cm $^{-2}$  s $^{-1}$  at 8.1 keV. Subsection A.2 of Appendix presents more details about the process of calculation.

### 2.3. Planck dataset

The Planck satellite, launched on 2009 May 14, is a third-generation space experiment aiming to study the Cosmic Microwave Background (CMB). It covers the observation wave-

length from  $350 \mu\text{m}$  to 1 cm and has a good angular resolution of  $\sim 5$  arcmin (Tauber et al. 2010).

We hoped to find counterparts, especially Molecular Clouds (MCs), of the six LHAASO UHE sources in far infrared band with Planck observation. The up-to-date Planck all-sky map at 857 GHz, obtained from the Planck Public Data Release 3 is presented in Fig. 2. Moreover, the original HEALPix fits table was converted into standard fits table in World Coordinate System (WCS) via the astronomical image toolkit **Montage** (Jacob et al. 2009), and the data within  $10^\circ \times 10^\circ$  ROIs centered on the six sources were extracted from it for more detailed analyses. As indicated by the yellow dashed circles on Fig. 2, no significant evidences of any counterparts close to these sources can be found, except for J0007+5659u. The exact environment of this source need to be further confirmed with Carbon monoxide (CO) observation.

The Planck catalog of compact sources has also been checked. However, no sources with position offset to the six sources smaller than  $0.3^\circ$  were found. The catalog can be accessed via the official website of NASA/IPAC Infrared Science Archive (IRSA)<sup>4</sup>.

<sup>2</sup> The Swift-XRT 2SXPS catalogue has been checked. The website is <https://www.swift.ac.uk/2SXPS/ulserv.php>

<sup>3</sup> The data were acquired from <https://heasarc.gsfc.nasa.gov/cgi-bin/W3Browse/swift.pl>

<sup>4</sup> <https://irsa.ipac.caltech.edu/frontpage/>

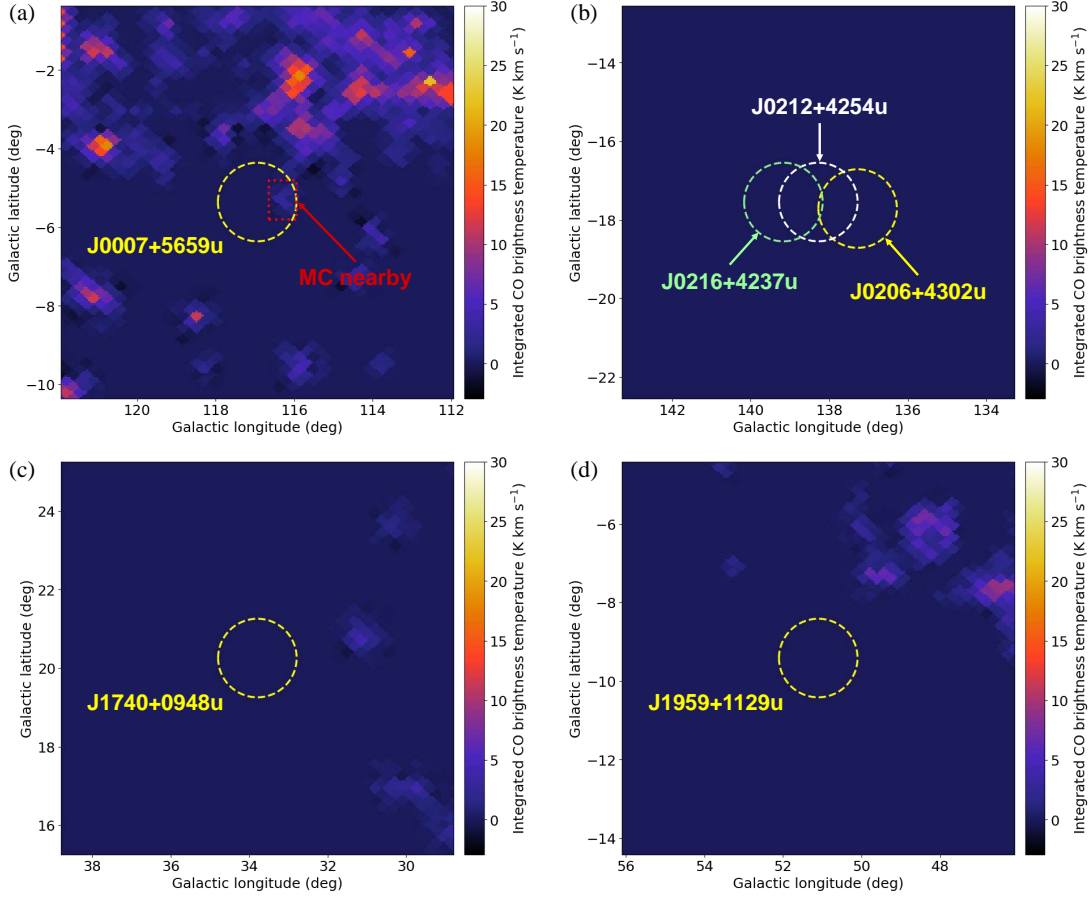


**Fig. 3.** Results of  $^{12}\text{CO}$  survey around the six LHAASO UHE sources. The data were velocity integrated with velocity coverage of  $\pm 47.1 \text{ km s}^{-1}$  (Dame & Thaddeus 2022). The positions of the six LHAASO sources are marked by yellow dashed circles with radius of  $1^\circ$ . The MC close to J0007+5659u is indicated by the red dashed box.

#### 2.4. LAMBDA dataset

As a double-check of the Planck observation, we also examined the Legacy Archive for Microwave Background Data Analysis (LAMBDA), and hope to find MCs associated with the six LHAASO UHE sources.

MCs provide abundant protons for inelastic interaction with CR protons, the so-called p-p interactions, which can result in high-energy  $\gamma$ -ray and neutrino emission (De Sarkar & Gupta 2022). One of the most common approaches to trace MC is to observe the  $^{12}\text{CO} \text{ J} = 1-0$  transition at 115 GHz (Su et al. 2019). The recent velocity-integrated  $^{12}\text{CO}$  map of the entire northern sky obtained by CfA 1.2 m telescope and its twin instrument in Chile (Dame & Thaddeus 2022) has been included in LAMBDA<sup>5</sup>. The HEALPix fits table of this  $^{12}\text{CO}$  map was used to obtain the  $^{12}\text{CO}$  distribution as MC distribution around the six sources. The same with Planck data processing, **Montage** toolkit was used for format conversion. Fig. 3 presents the results, only the LHAASO source J0007+5659u seems to have a faint MC around, while the other five sources are unlikely to be associated with any significant MCs. These results are consistent with the Planck observation.

The MC which might be associated with J0007+5659u covers a sky region of  $0.7^\circ \times 1^\circ$ . Using the  $^{12}\text{CO}$ -to- $\text{H}_2$  conversion factor of  $2 \times 10^{20} \text{ cm}^{-2} (\text{K km s}^{-1})^{-1}$  (Bolatto et al. 2013), the

averaged  $\text{H}_2$  column density of the MC is  $1.9 \times 10^{20} \text{ cm}^{-2}$ . The distance of the MC can be calculated online<sup>6</sup> via its Local Standard of Rest (LSR) velocity about  $-2 \text{ km s}^{-1}$  (Reid et al. 2016, 2019), extracted from the raw  $^{12}\text{CO}$  dataset<sup>7</sup>. The result is 0.7 kpc.

#### 2.5. IceCube neutrino dataset

High-energy neutrinos are the key to answer whether the  $\gamma$ -ray sources are hadronic or leptonic origins. Together with the multi-wavelength observations, from radio to  $\gamma$ -rays, they may shed light on the intrinsic properties of the Galactic sources and their environments.

IceCube neutrino observatory is a kilometer-scale neutrino experiment located at the south pole with 5160 Digital Optical Modules (DOMs) deployed under ice. It was constructed completely at December 18, 2010 and has been taking data since then (Aartsen et al. 2017). For the first time, IceCube detected high-energy neutrinos coming from extraterrestrial origins (Aartsen et al. 2013; Collaboration\* 2013). Recent years, IceCube has found evidence for neutrino sources, such as TXS 0506+056, NGC1068 and Galactic plane (Aartsen et al. 2018a,b; Abbasi et al. 2022, 2023b). Some correlation studies of IceCube neutrino and LHAASO sources have been performed, such as the

<sup>6</sup> <http://bessel.vlbi-astrometry.org/node/378>

<sup>7</sup> The raw data is available on <https://lweb.cfa.harvard.edu/rtdc/CO/NorthernSkySurvey/>

<sup>5</sup> The data can be downloaded from [https://lambda.gsfc.nasa.gov/product/foreground/fg\\_wco\\_dt2022\\_get.html](https://lambda.gsfc.nasa.gov/product/foreground/fg_wco_dt2022_get.html)

work done by Abbasi et al. (2023c); Fang & Halzen (2024); Li et al. (2024).

We finally searched the IceCube High-Energy Starting Events (HESE) data release of 12 years. The dataset contains 164 events that are reconstructed based on the latest ice model via **DirectFit** (Abbasi et al. 2023a). No significant association with an offset angle of  $2^\circ$  has been found for these six LHAASO sources. For the public data release of neutrino track-like events between April 6, 2008 and July 8, 2018, no significant excess was found. Therefore, the upper limits are obtained based on the information of exposure time, effective area and atmospheric background rate at the level of  $1 \times 10^{-9}$  erg cm $^{-2}$  s $^{-1}$  sr $^{-1}$  for the dumbbell-like structure (Aartsen et al. 2020; Abbasi et al. 2021).

### 3. Modeling research

#### 3.1. Leptonic modeling

As observed by the High-Altitude Water Cherenkov Observatory (HAWC) in 2017, the Geminga (PSR J0633+1746) has a significant TeV  $\gamma$ -ray halo around it with a hard spectral index of  $\sim 2.34$  (Abeysekara et al. 2017). It can be seen that the energy coverage and spectral index of the  $\gamma$ -ray halo around Geminga are similar to the six mysterious UHE sources observed by LHAASO. Thus, it is reasonable for us to regard Geminga as a reference leptonic model for the six LHAASO sources.

For a rapid rotation pulsar like Geminga, the relativistic wind generated by it can accelerate the environmental particles including electrons, and finally forms a bubble of shocked relativistic particles (Gaensler & Slane 2006), the so-called PWN. There are three typical mechanisms for the cooling of these relativistic electrons – synchrotron radiation, Inverse-Compton (IC) scattering and bremsstrahlung. When traveling in ambient magnetic field, the PWN electrons can emit synchrotron radiation with energy of several keVs. At higher energy band up to PeV, IC scattering will gradually becomes dominated, which means that it is the major contributor to the TeV  $\gamma$  photons we are interested in. The radiation field in IC scattering can be the CMB, far-infrared and near-infrared radiation or the visible light. Moreover, the collision between electrons and other particles can cause bremsstrahlung, whose contribution to UHE emission is lower than that of the IC scattering.

Considering Geminga PWN as a reference, and involving all the three electron cooling mechanisms into the model, we study the leptonic origins of the six LHAASO sources. During the study, the  $\gamma$ -ray source modeling package **GAMERA** (Hahn 2015), developed by the Max Planck Institute for Nuclear Physics in Heidelberg (MPIK), was used to calculate the leptonic spectra. The injection electrons of PWN were assumed to satisfy a power-law spectrum with an exponential cutoff. The function can be written as

$$\frac{dN}{dE} = N_e \left( \frac{E}{1 \text{ TeV}} \right)^{-\alpha_e} \exp\left(-\frac{E}{E_c}\right). \quad (1)$$

Where  $\alpha_e$  and  $E_c$  are the spectral index and cutoff energy, which are free parameters in our leptonic modeling research.  $N_e$  is the normalization factor depending on the total energy  $W_e$  of PWN electrons. The relationship between  $N_e$  and  $W_e$  is

$$W_e = N_e \int_{E_{\min}}^{E_{\max}} E \left( \frac{E}{1 \text{ TeV}} \right)^{-\alpha_e} \exp\left(-\frac{E}{E_c}\right) dE. \quad (2)$$

Here  $W_e$  was set as  $1.43 \times 10^{45}$  erg, corresponding to 0.01% of the total spin-down energy of Geminga (Fang et al. 2018).

**Table 2.** Best-fit parameters in leptonic modeling

Source	$\alpha_e$	$E_c$ (TeV)	$d$ (kpc)
J0007+5659u	1.84	133.95	1.94
J0206+4302u	1.84	226.83	2.62
J0212+4254u	1.80	234.10	3.99
J0216+4237u	1.79	232.83	3.38
J1740+0948u	1.88	130.23	1.54
J1959+1129u	1.82	215.54	2.64

The minimum and maximum energy of PWN electrons  $E_{\min}$  and  $E_{\max}$  was chosen to be 0.1 GeV and 10 PeV to match the KM2A data. The strength of magnetic field associated with the six sources for calculating the intensity of synchrotron radiation was set as  $1 \mu\text{G}$  to match the X-ray observation results of Swift-XRT. It was a reasonable value in Galactic halo (Jansson & Farrar 2012). The radiation fields in IC scattering were assumed to be CMB (temperature equals to 2.73 K and energy density equals to  $0.25 \text{ eV cm}^{-3}$ ), far-infrared radiation (temperature equals to 40 K and energy density equals to  $1 \text{ eV cm}^{-3}$ ), near-infrared radiation (temperature equals to 500 K and energy density equals to  $0.4 \text{ eV cm}^{-3}$ ) and visible light (temperature equals to 3500 K and energy density equals to  $1.9 \text{ eV cm}^{-3}$ ) (Popescu et al. 2017; Zhang et al. 2021). The ambient particle number density around PWN for bremsstrahlung calculation was assumed to be  $0.1 \text{ cm}^{-3}$  (De Sarkar & Gupta 2022). The distance  $d$  between PWN and Earth, which determined the total flux intensity while  $W_e$  was fixed, was left free in our model.

As a summary, the free parameters to be fitted in our model were  $\alpha_e$ ,  $E_c$  and  $d$ . The Monte Carlo Markov Chain (MCMC) method was used for the fitting (Geyer 1992). In this process, the input of our model was the energy of  $\gamma$  photon and the output was the SED. The experimental data were the fitted KM2A SEDs (Cao et al. 2024) of the six sources presented by the LHAASO collaboration. For leptonic modeling, the upper limits of SEDs at different energy bands based on Fermi-LAT (see Subsection 2.1), Swift (see Subsection 2.2) and WCDA (Cao et al. 2024) datasets were utilized to constraint the fitting. A punishment on likelihood for upper limit break was added into the likelihood function of MCMC fitting. Before running the MCMC fitting, the scientific calculation toolkit **Scipy** was used to obtain the start point of Markov Chain. Each chain contained 2000 steps and the first 200 steps were chosen as burn-in steps. The entire calculation and fitting were conducted under **Python3** environment.

Fig. 4 shows the results of our leptonic modeling study. The best-fit  $\alpha_e$ ,  $E_c$  and  $d$  are given in Table 2. All the six sources have a similar best-fit spectral index of  $\sim 1.8$ . The best-fit cutoff energies of J0206+4302u, J0212+4254u, J0216+4237u and J1959+1129u are also similar, which is about 100 TeV higher than those of J0007+5659u and J1740+0948u. All the six sources have cutoff energies beyond 100 TeV. Compared with previous works on PWN leptonic modeling (Ding et al. 2021; De Sarkar & Gupta 2022), our results are reasonable, inferring the possibility of the six LHAASO UHE sources belong to leptonic origin.

On Fig. 4, the expected sensitivity of  $3 \times 10^4$  seconds observation with the EUROPEAN PHOTON IMAGING CAMERA (EPIC) integrated on XMM-Newton in the energy range of 0.5~10 keV is also presented<sup>8</sup>. It can be seen that, the sen-

<sup>8</sup> The sensitivity is based on the XMM-Newton Users Handbook, which can be downloaded from [http://xmm-tools.cosmos.esa.int/external/xmm\\_user\\_support/documentation/uhb/XMM\\_UHB.pdf](http://xmm-tools.cosmos.esa.int/external/xmm_user_support/documentation/uhb/XMM_UHB.pdf)

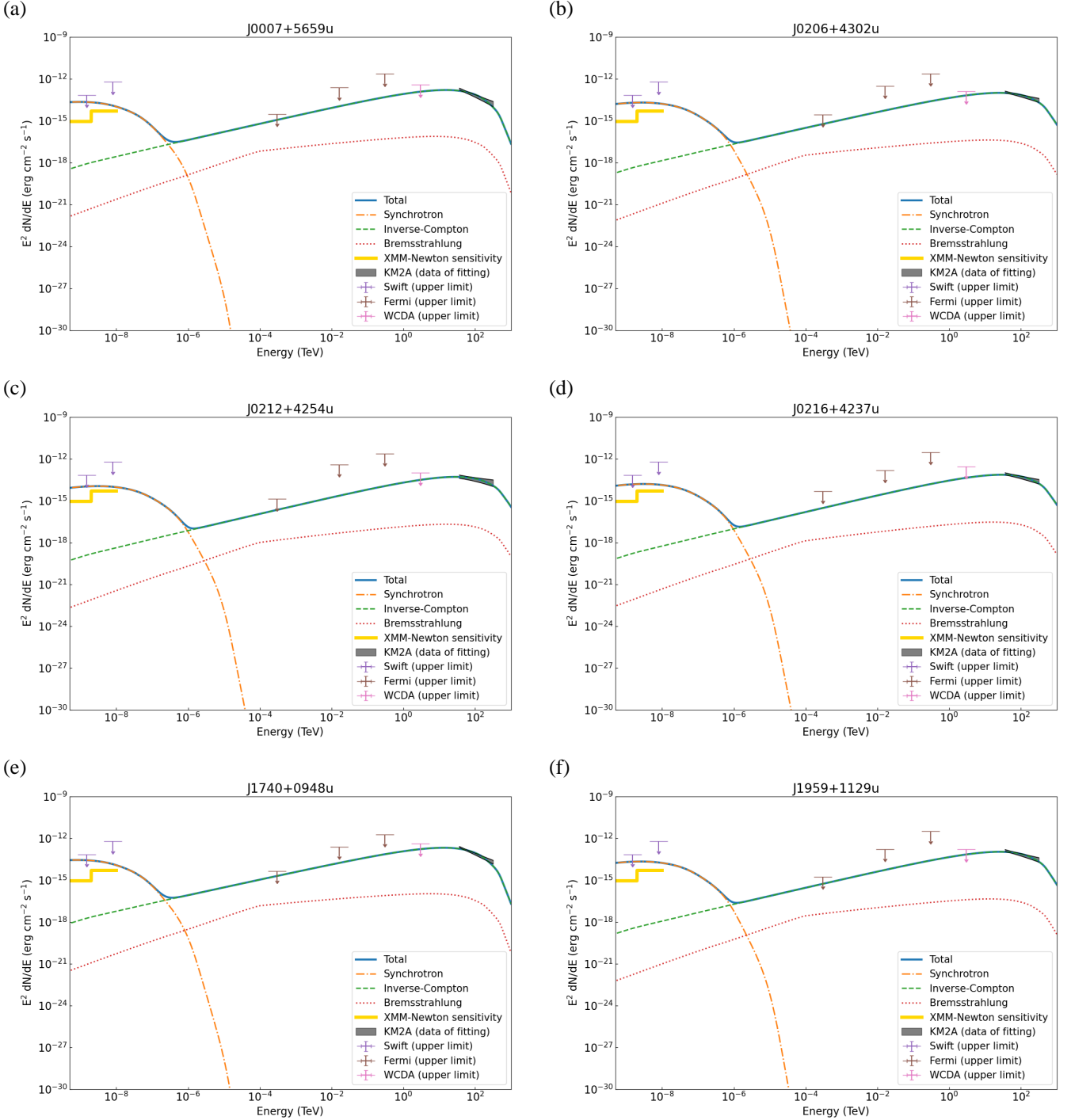


**Fig. 4.** Results of leptonic modeling. (a) The result of J0007+5659u. The blue line represents the total SED of  $\gamma$ -ray. The dashed lines with different colors are the SEDs contributed from synchrotron radiation, IC scattering and bremsstrahlung. The arrows pointing down stand for the upper limits obtained from the observations of Swift, Fermi-LAT and WCDA. The expected sensitivity of  $3 \times 10^4$  seconds' observation with EPIC-pn of XMM-Newton has been shown in the thick golden line. The fitted SED of KM2A data with error bar is displayed by a butterfly plot filled in black. (b)-(f) are the results of J0206+4302u, J0212+4254u, J0216+4237u, J1740+0948u and J1959+1129u, respectively.

sitivity of XMM-Newton observation within such time-scale is below the expected SED in our leptonic model. That means, with the observation data of XMM-Newton, it is possible to examine if the six sources originate from leptonic interaction. The further researches on these sources with sensitive X-ray telescopes like XMM-Newton are expected.

### 3.2. Hadronic modeling

Except for the three cooling mechanisms of relativistic electrons, the p-p interaction also plays an important role in the generation of UHE  $\gamma$ -rays. In general, when CR inject into an MC, the inelastic collisions among the accelerated CR protons and cold MC protons will produce light mesons. The decay of these light mesons, such as  $\pi^0 \rightarrow \gamma\gamma$  or  $\eta \rightarrow \gamma\gamma$ , is the major origin of

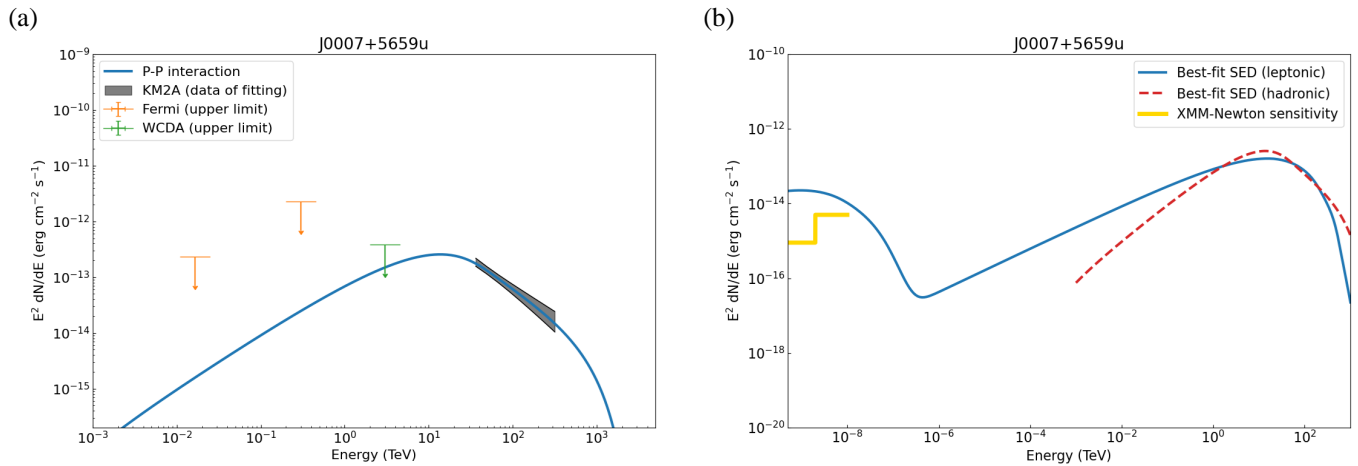


**Fig. 5.** Results of hadronic modeling on J0007+5659u. (a) The best-fit result compared with multi-wavelength upper limits. The blue line represents for the SED of  $\gamma$ -ray generated by p-p interaction. The arrows pointing down stand for the upper limits of SED according to the observations of Fermi-LAT and WCDA. The fitted SED of KM2A data with error bar is displayed by a butterfly plot filled in black. (b) Comparison between the leptonic and hadronic best-fit results. The expected sensitivity of  $3 \times 10^4$  seconds' observation with EPIC-pn of XMM-Newton is shown by the thick golden line.

UHE  $\gamma$  photons in hadronic scenario. If an UHE  $\gamma$ -ray source is confirmed as hadronic origin, the study combined with neutrino detection will be very helpful to reveal the exact physical mechanisms behind it.

In the case of p-p interaction, the MCs providing cold protons are essential. According to Subsection 2.3 and 2.4, only the LHAASO source J0007+5659u might have associated MCs. Thus, we merely study a p-p interaction model on J0007+5659u to examine the possibility of this source belong to hadronic scenario. The **GAMERA** toolkit (Hahn 2015) was also used here. The injected CR protons were assumed to have a simple power-law spectrum in the form of

$$\frac{dN}{dE} = N_p \left( \frac{E}{1 \text{ TeV}} \right)^{-\alpha_p}. \quad (3)$$

Where  $N_p$  is the normalization factor depending on the total energy of injected protons  $W_p$ , similar to that in leptonic scenario. As the area and averaged  $H_2$  column density of the MC associated with J0007+5659u have been extracted in Subsection 2.4, the energy density  $U_p$  of injected protons equals to  $W_p/V$ , where  $V$  denotes the volume of MC, is the major parameter that decides the intensity of  $\gamma$  photon flux originated from p-p interaction.  $\alpha_p$  is the spectral index of injected protons. It was also set as a free parameter in model fitting. The maximum energy  $E_{\text{max}}^p$  of injected protons was chosen to be the CR knee energy of  $\sim 3.16 \times 10^3$  TeV, while the minimum energy  $E_{\text{min}}^p$  was another free parameter to be fitted. The column density and distance of the MC was the same with that in Subsection 2.4.

Similar to leptonic modeling, there are three free parameters to be fitted in our p-p interaction model –  $U_p$ ,  $\alpha_p$  and  $E_{\text{min}}^p$ . Also, an MCMC method with each chain containing 2000 steps (the first 200 steps were burn-in steps) was utilized to fit the KM2A SED (Cao et al. 2024) of J0007+5659u as experimental data. The upper limits of SEDs at different energy bands based on Fermi-LAT (see Subsection 2.1) and WCDA (Cao et al. 2024) datasets were added into the model to constraint the fitting. The upper limits given by IceCube dataset (see Subsection 2.5) were much higher than those of Fermi-LAT and WCDA. Thus, they were not involved in the fitting. Fig. 5 (a) shows the result of fitting. The best-fit  $U_p$  is  $0.54 \text{ eV cm}^{-3}$ , about 2.5 times lower

than the average value in the Milky Way and approximate to that of Large Magellanic Cloud (LMC) (Yoast-Hull et al. 2016). The best-fit  $\alpha_p$  is 3.12, which is reasonable for CR protons (De Sarkar & Gupta 2022). The best-fit  $E_{\text{min}}^p$  is  $\sim 68.73$  TeV.

The result of p-p interaction model fitting might indicate a scenario where a hidden Supernova Remnant (SNR) with relative long Sedov time (De Sarkar & Gupta 2022) is close to the MC associated with J0007+5659u. The SNR traps low energy CR protons in a small region and leads to the lonely  $> 25$  TeV emission of J0007+5659u. However, the large position offset about  $0.7^\circ$  between the MC and J0007+5659u and the low probability of an SNR at a distance of 0.7 kpc have never been observed reduce the reliability of this explanation.

Fig. 5 (b) shows the comparison between the leptonic and hadronic best-fit SED of J0007+5659u as well as the sensitivity of  $3 \times 10^4$  seconds' XMM-Newton observation. It is expected that the results of XMM-Newton observation can distinguish the leptonic origin of J0007+5659u from the hadronic origin.

The process of light mesons decay after p-p interaction is always accompanied by the production of neutrinos via the decay of pions and muons. Thus, neutrino detection is also essential for identifying the origin of a  $\gamma$ -ray source and can provide useful supplemental information about the source. According to our hadronic modeling research, the expected neutrino SED from J0007+5659u is about an order of magnitude lower than the sensitivity limit of IceCube-Gen2 at 10 TeV and about two orders of magnitude lower at 100 TeV. It seems unlikely to observe the neutrinos generated by this source at present, even the hadronic origin has been confirmed. However, with the improvement on technology, there are still prospects of detecting associated neutrinos with some other proposed next generation neutrino observatories, like TRIDENT (Ye et al. 2022) and NEON (Zhang et al. 2023). The details of neutrino SED calculation are provided in Section B of Appendix.

#### 4. Traveling-PWN modeling attempt

One of the most attractive things presented by the LHAASO catalog is the dumbbell-like structure (see the left bottom of Figure 10 in Cao et al. (2024)) consisting of J0206+4302u,



J0212+4254u and J0216+4237u. The similarities in position and spectral shape of the three sources suggest a physical association among them. The low UHE  $\gamma$ -ray source density at such high galactic latitude makes this assumption more acceptable. Some previous works have tried some theoretical explanations like the asymmetric propagation of UHE electrons due to the turbulent magnetic field around pulsars to explain this structure (Bao et al. 2024), and considering PSR J0218+4232 as the counterpart. Moreover, the relativistic jet from microquasar can also be a candidate for the origin of the extended structure. However, the present observation on this structure haven't shown enough evidence. In this section, we attempt to use the traveling-PWN model containing one traveling-PWN, two traveling-PWNe and three PWNe under the isotropic and homogeneous diffusion condition to explain the origin of the dumbbell-like structure.

#### 4.1. Single traveling-PWN modeling attempt

We firstly discuss the hypothesis that the dumbbell-like structure was formed by a single traveling-PWN in this subsection. As only one corresponding pulsar was required, there was no need to consider the probability of pulsars spatial coincidence by chance. Similar to the propagation of CR particles, the relativistic electrons accelerated by the central pulsar of a PWN also have spatial diffusion. This process is accompanied by the proper-motion of the central pulsar and leaves  $\gamma$ -ray and X-ray filaments. Based on the statistical study, a pulsar can travel with velocity up to  $\sim 1600 \text{ km s}^{-1}$  (Hobbs et al. 2005). If the distance  $d$  between the PWN and Earth is short enough (e.g.,  $< 0.5 \text{ kpc}$ ), with such proper-motion velocity, the  $\gamma$ -ray filament can be significant enough to be detected by KM2A and might be misunderstood as three point-like sources.

The diffusion of electrons emitted from a PWN can be described by a diffusion equation (Delahaye et al. 2008, 2010; Fang et al. 2018; Zhang et al. 2021; Fang & Bi 2022)

$$\frac{\partial \psi}{\partial t} - \nabla \cdot [D(E)\nabla \psi] - \frac{\partial}{\partial E}[b(E)\psi] = q(\mathbf{r}, E, t), \quad (4)$$

where  $\psi(\mathbf{r}, E, t)$  denotes the electron number density per unit energy.  $D(E) \equiv D_0 \epsilon^\delta$  is the energy-dependent diffusion coefficient assumed to be isotropic and homogeneous (Zhang et al. 2021; Fang & Bi 2022).  $D_0$  represents for the normalization factor.  $\epsilon \equiv E/E_d$  is the dimensionless energy, where  $E_d = 1 \text{ GeV}$  (Delahaye et al. 2008, 2010).  $b(E)$  describes the energy-loss rate of electrons due to synchrotron radiation and IC scattering on cosmic radiation fields (Delahaye et al. 2008). The exact form of  $b(E)$ , considering the Klein-Nishina effect (Nakar et al. 2009), can be written as (Zhang et al. 2021)

$$\begin{aligned} b(E) &= -\frac{dE}{dt} \\ &= \frac{4}{3} \sigma_T c \left( \frac{E}{m_e c^2} \right)^2 \left[ U_B + \frac{U_{\text{ph}}}{\left(1 + \frac{4E\epsilon_0}{m_e^2 c^4}\right)^{3/2}} \right] \\ &= \frac{4}{3} \sigma_T c \epsilon^2 \left( \frac{E_d}{m_e c^2} \right)^2 \left[ U_B + \frac{U_{\text{ph}}}{\left(1 + \frac{4E_d \epsilon \epsilon_0}{m_e^2 c^4}\right)^{3/2}} \right]. \end{aligned} \quad (5)$$

Here  $\sigma_T$  is the Thomson cross section.  $c$  denotes the velocity of light.  $U_B = B^2/(2\mu_0)$  is the energy density of magnetic field, where  $B$  represents for the strength of magnetic field and  $\mu_0$  stands for the permeability of vacuum.  $U_{\text{ph}}$  is the energy density of radiation field.  $\epsilon_0 = 2.82k_b T$  is the typical photon energy

of the blackbody/graybody target radiation field, as  $k_b$  and  $T$  represent for the Boltzmann constant and temperature. Assuming PWN as a constant injection source, the source term  $q(\mathbf{r}, E, t)$  is expected to have a power-law spectrum with an exponential cutoff

$$\begin{aligned} q(\mathbf{r}, E, t) &= q_0 \left( \frac{E}{1 \text{ GeV}} \right)^{-\Gamma} \exp\left(-\frac{E}{E_c}\right) \delta(\mathbf{r} - \mathbf{r}_0 - \mathbf{v}t) \\ &= q_0 \epsilon^{-\Gamma} \exp\left(-\frac{E_d}{E_c} \epsilon\right) \delta(\mathbf{r} - \mathbf{r}_0 - \mathbf{v}t). \end{aligned} \quad (6)$$

Where  $\Gamma$  is the spectral index of injection spectrum.  $\mathbf{r}_0$  denotes the position of the traveling PWN at  $t = 0$  and  $\mathbf{v}$  stands for the proper-motion velocity of the central pulsar.  $q_0$  is the normalization factor depending on the total energy of PWN injection, which was denoted by  $W_e$  in the previous text. The relationship between  $q_0$  and  $W_e$  is similar to equation (2), with  $N_e$  replaced by  $q_0$ . The  $W_e$  is a fraction  $\eta$  of the total spin-down energy  $W_0$  of the associated pulsar, while  $W_0$  satisfies the equation (Gaensler & Slane 2006; Fang & Bi 2022)

$$W_0 = \dot{\xi} t_a \left(1 + \frac{t_a}{\tau_0}\right) \left(\frac{t_a + \tau_0}{t + \tau_0}\right)^{\frac{n+1}{n-1}}. \quad (7)$$

Here  $\dot{\xi}$  denotes the rotational kinetic energy dissipation rate or called ‘‘spin-down luminosity’’ of the pulsar at  $t = t_a$ , while  $t_a$  represents for the evolutionary time of the pulsar. In our model, the spin-down luminosity decays with time following Ding et al. (2021), meanwhile,  $\Gamma$  and  $E_c$  of the accelerated electrons remain constant through the traveling history.  $\tau_0 \sim 10 \text{ kyr}$  is the typical spin-down luminosity decay time (Ding et al. 2021). Based on equation (2), (5), (6) and (7), the full expansion of equation (4) can be expressed as

$$\begin{aligned} &\frac{\partial \psi}{\partial t} - D_0 \left( \frac{\epsilon}{10^5} \right)^\delta \Delta \psi - \frac{\partial}{\partial \epsilon} \left( \frac{\epsilon^2}{\tau_l} \psi \right) \\ &= q(\mathbf{r}, \epsilon, t) \\ &= \frac{\eta \dot{\xi}}{E_d^2 I_\epsilon} \left(1 + \frac{t_a}{\tau_0}\right) \left(\frac{t_a + \tau_0}{t + \tau_0}\right)^{\frac{n+1}{n-1}} \\ &\quad \times \epsilon^{-\Gamma} \exp\left(-\frac{E_d}{E_c} \epsilon\right) \delta(\mathbf{r} - \mathbf{r}_0 - \mathbf{v}t) \gamma_n(t), \end{aligned} \quad (8)$$

and

$$\frac{1}{\tau_l} = \frac{4}{3} \sigma_T c \frac{E_d}{m_e^2 c^4} \left[ U_B + \frac{U_{\text{ph}}}{\left(1 + \frac{4E_d \epsilon \epsilon_0}{m_e^2 c^4}\right)^{3/2}} \right], \quad (9)$$

$$I_\epsilon = \int_{\epsilon_{\min}}^{\epsilon_{\max}} \epsilon_1^{1-\Gamma} \exp\left(-\frac{E_d}{E_c} \epsilon_1\right) d\epsilon_1. \quad (10)$$

Where  $\epsilon_{\min}$  and  $\epsilon_{\max}$  represent for the constraints on the energy of electrons emitted by PWN.  $\gamma_n(t)$  is a step function, which returns 1 while  $t \geq 0$ .

As the diffusion coefficient is isotropic and homogeneous, we can use the Green function method to solve equation (8) analytically. For our model, the Green function can be written as (Fang & Bi 2022)

$$G(\mathbf{r}, t \leftarrow \mathbf{r}_s, t_s) = \frac{b(\epsilon^*)}{b(\epsilon)} \frac{1}{(\pi \lambda^2)^{3/2}} \exp\left[-\frac{(\mathbf{r} - \mathbf{r}_s)^2}{\lambda^2}\right]. \quad (11)$$

Here  $\mathbf{r}_s$  and  $t_s$  represent for the position and time of an arbitrary electron injection in Green function method. The diffusion

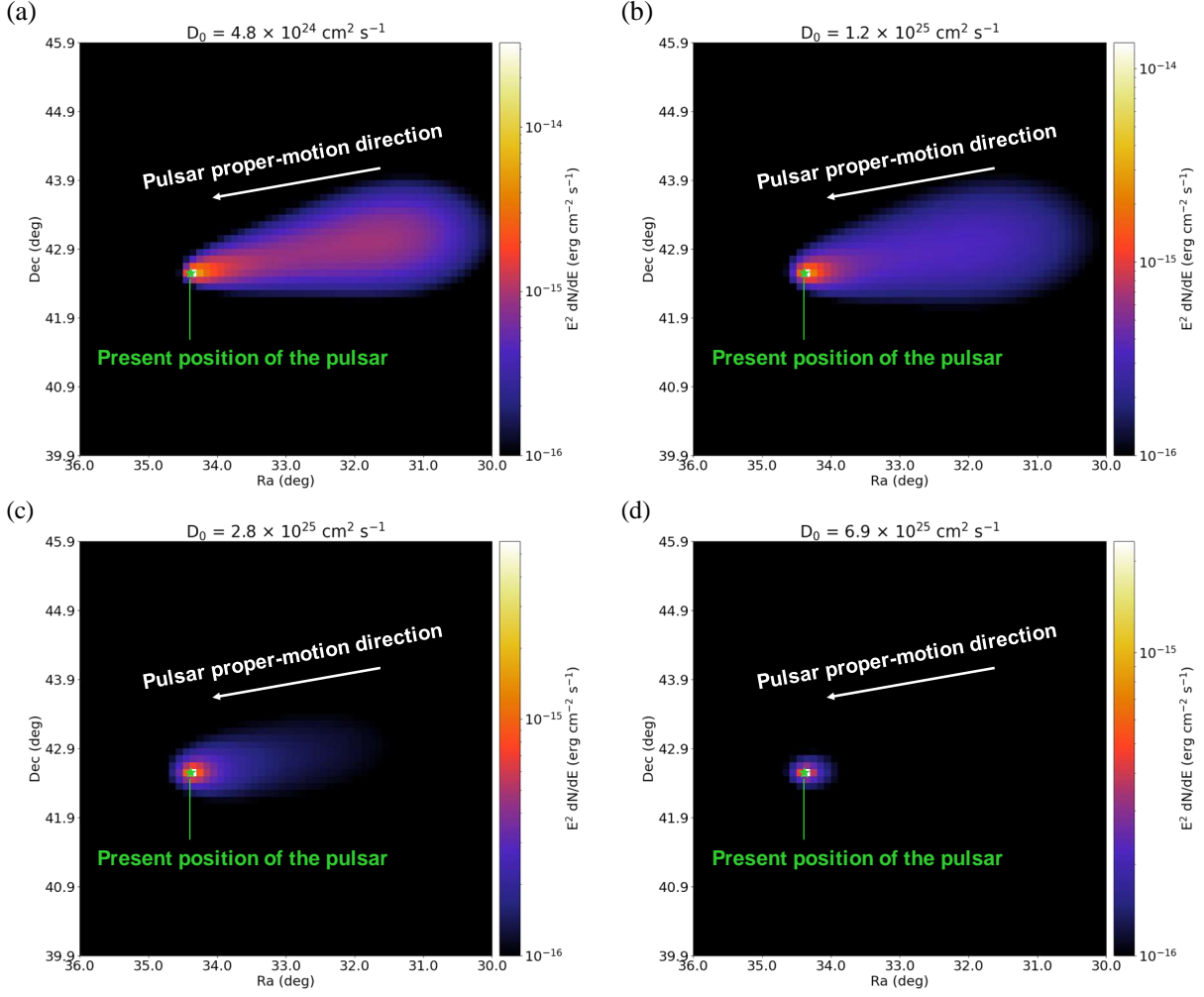


**Fig. 6.** The  $\gamma$ -ray flux intensity maps at energies over 50 TeV with different  $D_0$ . (a)-(d) give the results for  $D_0 = 4.8 \times 10^{24} \text{ cm}^2 \text{ s}^{-1}$ ,  $D_0 = 1.2 \times 10^{25} \text{ cm}^2 \text{ s}^{-1}$ ,  $D_0 = 2.8 \times 10^{25} \text{ cm}^2 \text{ s}^{-1}$  and  $D_0 = 6.9 \times 10^{25} \text{ cm}^2 \text{ s}^{-1}$ , respectively. For comparing with the physical image shown in the LHAASO catalog, the coordinate system used here is the J2000 equatorial frame. Other parameters used in the calculation are  $d = 0.375 \text{ kpc}$  and  $v = 1600 \text{ km s}^{-1}$ . The white arrow indicates the proper-motion direction of the pulsar, while the green star shape marks the present position of the pulsar.

length  $\lambda$  and modified dimensionless energy  $\epsilon^*$  have the expressions of

$$\lambda^2 = \frac{4D_0\tau_l}{\delta - 2}(\epsilon^{*\delta-1} - \epsilon^{\delta-1}), \quad (12)$$

$$\epsilon^* = \frac{\epsilon}{1 - \epsilon/\tau_l(t - t_s)}. \quad (13)$$

For a free boundary condition, the analytical solution of equation (8) based on Green function method can be expressed as

$$\psi(\mathbf{r}, \epsilon, t) = \int_{\mathbb{R}^3} d^3\mathbf{r}_s \int_{t_i}^t dt_s G(\mathbf{r}, t \leftarrow \mathbf{r}_s, t_s) q(\mathbf{r}_s, \epsilon^*, t_s), \quad (14)$$

where  $t_i = \max\{t - \tau_l/\epsilon, 0\}$  is the time of injection.  $\tau_l/\epsilon = E/b(E)$  describes the cooling timescale of injected electrons (Zhang et al. 2021).

The morphology of PWN electrons diffusion combined with proper-motion is depending on several parameters, as the major parameters are the diffusion coefficient  $D(E)$ , distance  $d$  and proper-motion velocity  $v$ . Thus, we firstly explore the influence of varying  $D_0$ ,  $d$  and  $v$ . From equation (12), it can be seen that the diffusion length of electron is in direct proportion to  $\sqrt{D_0}$ .

With a higher  $D_0$ , the electrons will diffuse more rapidly, result in the decrease of local electron number density and lower  $\gamma$ -ray flux intensity. The parameters  $d$  and  $v$  mainly influence the evolutionary time  $t_a$  of pulsar. To form the  $> 25 \text{ TeV}$  dumbbell-like structure,  $t_a$  needs to be shorter than the cooling timescale of  $> 100 \text{ TeV}$  electrons which are essential to the generation of  $> 25 \text{ TeV}$   $\gamma$  photons. Moreover,  $d$  and  $v$  also have impact on the source extension size and observed  $\gamma$ -ray flux intensity.

The spatial distribution of electron number density per unit energy can be directly calculated by equation (14) and transformed into  $\gamma$ -ray flux intensity map with the magnetic field and radiation field model used in Subsection 3.1. Fig. 6 presents the  $\gamma$ -ray flux intensity maps at energies over 50 TeV with different  $D_0$ . Here, we assume the direction of pulsar proper-motion is perpendicular to the Line of Sight (LOS).  $D_0$  varies from the minimum observed value of  $4.8 \times 10^{24} \text{ cm}^2 \text{ s}^{-1}$  around HESS J1026–582 (Di Mauro et al. 2020) to the typical value of  $6.9 \times 10^{25} \text{ cm}^2 \text{ s}^{-1}$  around Geminga. The  $D_0$  of  $4.8 \times 10^{24} \text{ cm}^2 \text{ s}^{-1}$  is far out of the one standard deviation interval of the statistical result on diffusion coefficients around 27 pulsars (Di Mauro et al. 2020), which is capable under a strong magnetic turbulence condition (Shalchi 2009; Hussein & Shalchi 2014). In Fig.

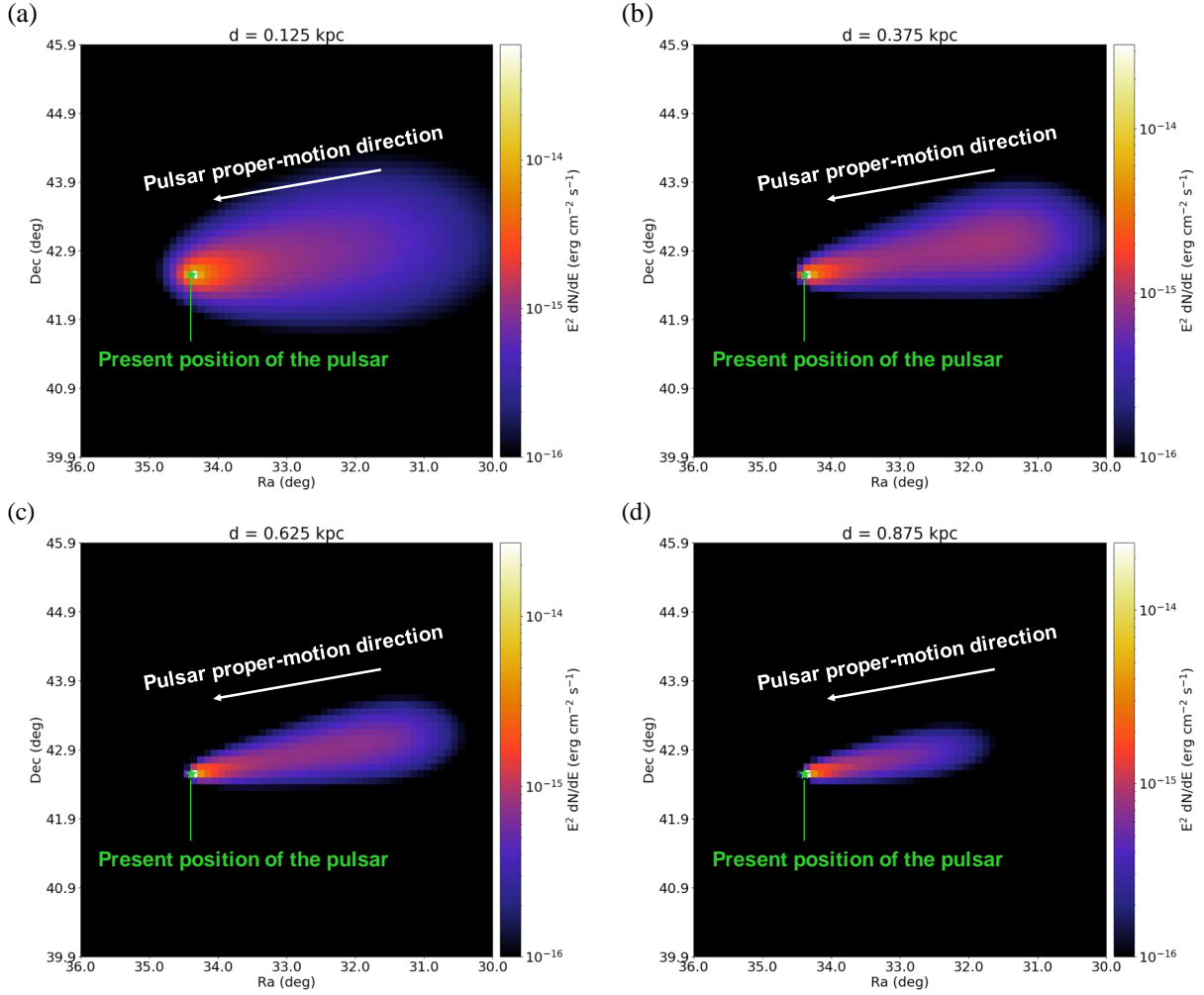


**Fig. 7.** The  $\gamma$ -ray flux intensity maps at energies over 50 TeV with different  $d$ . (a)-(d) give the results for  $d = 0.125$  kpc,  $d = 0.375$  kpc,  $d = 0.625$  kpc and  $d = 0.875$  kpc, respectively. Other parameters used in the calculation are  $D_0 = 4.8 \times 10^{24} \text{ cm}^2 \text{ s}^{-1}$  and  $v = 1600 \text{ km s}^{-1}$ .

6, the lower bound of  $\gamma$ -ray SED is set as  $1 \times 10^{-16} \text{ erg cm}^{-2} \text{ s}^{-1}$ . As shown by Fig. 6, with the increase of  $D_0$ , the rapid diffusion of electrons will lead to the decrease of  $\gamma$ -ray flux intensity and result in the smaller (not larger due to the SED cut) and dimmer TeV  $\gamma$ -ray halo. Thus, for the single traveling-PWN scenario, only if the diffusion coefficient is more than an order of magnitude lower than that around Geminga, the TeV  $\gamma$ -ray halo generated by the PWN can cover the entire sky region of the dumbbell-like structure as shown in Fig. 6 (a).

The  $\gamma$ -ray flux intensity maps at energies over 50 TeV with different  $d$  are presented in Fig. 7. Also, the direction of pulsar proper-motion is assumed to be perpendicular to the LOS.  $d$  varies from 0.125 kpc to 0.875 kpc, which are reasonable values. The same as Fig. 6, the lower bound of  $\gamma$ -ray SED is set as  $1 \times 10^{-16} \text{ erg cm}^{-2} \text{ s}^{-1}$  in Fig. 7. As shown by the figure, when  $d$  is too short and result in excessively short  $t_a$ , the energetic electrons injected recently will generate a huge and bright  $\gamma$ -ray blob as no double-peak structure like shown in the LHAASO significance map can be observed. With the increase of  $d$ ,  $t_a$  can be longer than the cooling timescale of UHE electrons. Due to the cooling of electrons injected previously, the TeV  $\gamma$ -ray halo will no longer cover the entire sky region of the dumbbell-like structure. Thus, for the single traveling-PWN scenario, the dumbbell-like

structure can only be formed by a PWN at proper distance as shown in Fig. 7 (b).

At last, the  $\gamma$ -ray flux intensity maps at energies over 50 TeV with different  $v$  are presented in Fig. 8. Here,  $v$  varies from a common value of  $400 \text{ km s}^{-1}$  to the maximum observed value of  $1600 \text{ km s}^{-1}$  (Hobbs et al. 2005). It can be seen on Fig. 8 that even the distance is short enough, for generating the dumbbell-like structure, the PWN still needs to travel with an incredible velocity over  $1200 \text{ km s}^{-1}$  to avoid the cooling of UHE electrons. As the proper-motion velocity increased to  $1600 \text{ km s}^{-1}$ , the morphology gradually becomes double peaked.

According to our exploration on the influence of  $D_0$ ,  $d$  and  $v$ , we set  $D_0 = 4.8 \times 10^{24} \text{ cm}^2 \text{ s}^{-1}$ ,  $d = 0.375$  kpc and  $v = 1600 \text{ km s}^{-1}$  for the single traveling-PWN scenario. Based on these parameters and the magnetic field and radiation field model used before, the  $\gamma$  photon counts map at energies over 25 TeV is plotted in Fig. 9 (a). Here, we assumed the PWN travel from (RA =  $30.8000^\circ$ , DEC =  $43.1850^\circ$ ) to (RA =  $34.4000^\circ$ , DEC =  $42.5575^\circ$ ) during the evolution. The other major parameters used are presented in Table 3. The positions of the three LHAASO sources and the only known pulsar PSR J0218+4232 are marked on Fig. 9 (a). As presented by the figure, PSR J0218+4232 is very close to the present position of the hypothetical pulsar in our model. However, it seems unlikely for PSR J0218+4232 to

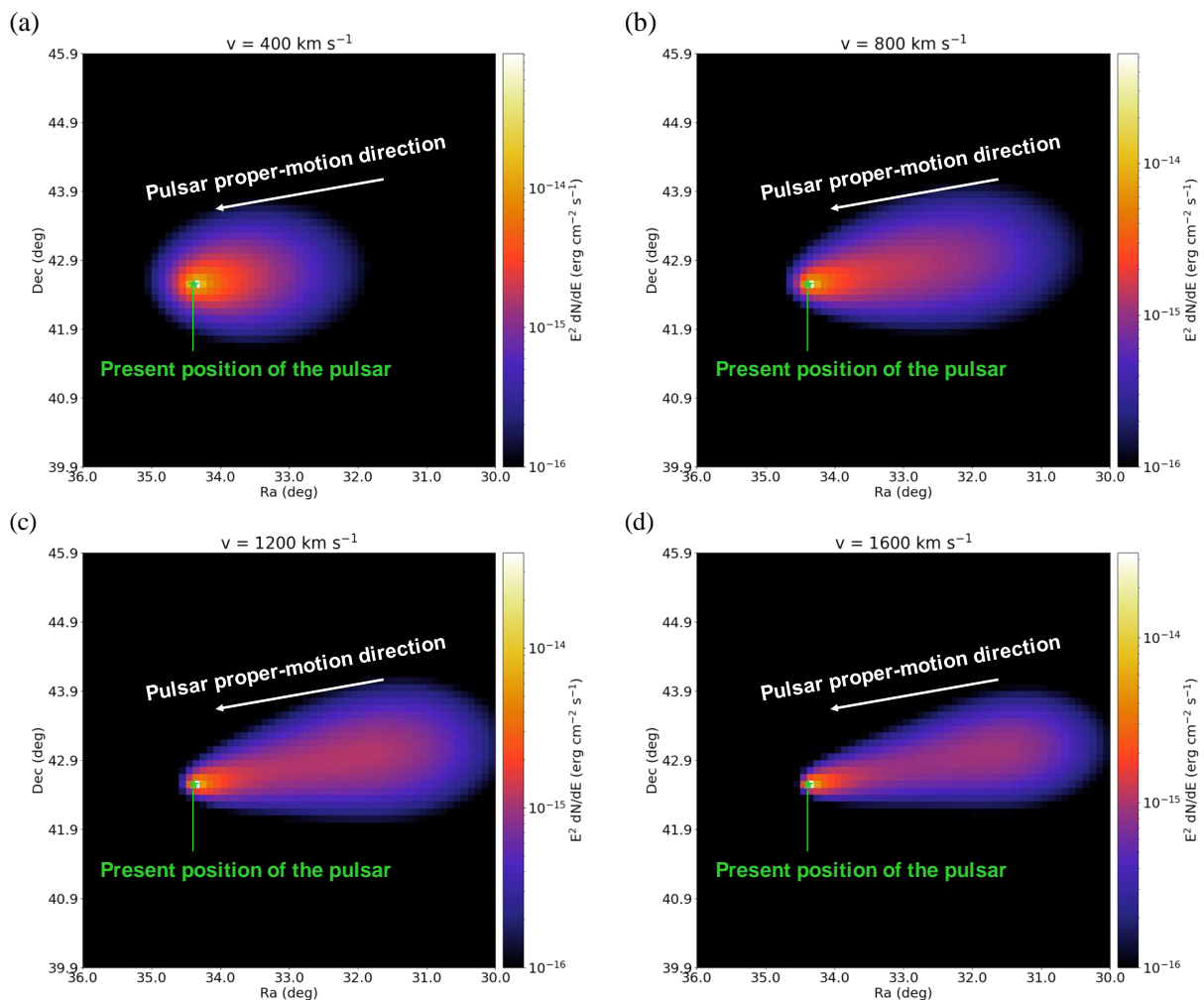


**Fig. 8.** The  $\gamma$ -ray flux intensity maps at energies over 50 TeV with different  $v$ . (a)-(d) give the results for  $v = 400 \text{ km s}^{-1}$ ,  $v = 800 \text{ km s}^{-1}$ ,  $v = 1200 \text{ km s}^{-1}$  and  $v = 1600 \text{ km s}^{-1}$ , respectively. Other parameters used in the calculation are  $D_0 = 4.8 \times 10^{24} \text{ cm}^2 \text{ s}^{-1}$  and  $d = 0.375 \text{ kpc}$ .

be the hypothetical pulsar, since the distance (Cao et al. 2024) and proper-motion velocity (Du et al. 2014) of this pulsar is far out of the reasonable bound for generating the dumbbell-like structure. More discussions about the potential contributions from PSR J0218+4232 will be provided in the next subsection.

By considering the residual CRs and Galactic  $\gamma$ -ray Emission (GDE) background of LHAASO (Cao et al. 2024) and applying a Gaussian smooth with  $1\sigma = 0.2^\circ$ , it is not difficult to predict the significance map seen from LHAASO based on the  $\gamma$  photon counts map. The  $1\sigma$  value used here is similar to that of the LHAASO Point Spread Function (PSF)  $> 25 \text{ TeV}$  (Hou et al. 2024). Figure 9 (b) shows the calculated significance map at energies over 25 TeV. As a result, assuming an extremely low diffusion coefficient and an ultra fast proper-motion velocity of the central pulsar, the filament of a single traveling-PWN generated by the isotropic and homogeneous diffusion of electrons has the prospect of exhibiting a dumbbell-like shape approximate to the extended structure observed by KM2A. Comparing Figure 9 (b) with Figure 9 (a), it can be found that the western  $> 25 \text{ TeV}$  blob (J0206+4302u) is formed by the diffused electrons from the central pulsar with higher spin-down luminosity at the early time, while the eastern  $> 25 \text{ TeV}$  blob (J0216+4237u) is originated from the fresh PWN electrons injected recently and extended with the LHAASO PSF.

**Table 3.** Major parameters used for the single traveling-PWN modeling attempt

Parameter	Value	Parameter	Value
$\dot{\xi}$ ( $\text{erg s}^{-1}$ )	$3.25 \times 10^{34}$	$\eta$	$3.4 \times 10^{-7}$
$D_0$ ( $\text{cm}^2 \text{ s}^{-1}$ )	$4.8 \times 10^{24}$	$\delta$	0.33
$E_c$ (TeV)	800	$n$	2
$v$ ( $\text{km s}^{-1}$ )	1600	$\Gamma$	1.8
$d$ (kpc)	0.375	$\epsilon_{min}$	0.1
$t_a$ (kyr)	14.6	$\epsilon_{max}$	$1.0 \times 10^7$

The SEDs of  $\gamma$ -ray at the positions of the three LHAASO sources were also calculated, and compared with the fitted SEDs of KM2A and upper limits given by the previous multi-wavelength and multi-messenger study. For the calculation on each source, all the  $\gamma$  photons  $> 25 \text{ TeV}$  within a circle region centered on it were involved. The radius of the circle region is  $0.5^\circ$ , the same with that of the LHAASO seeds used for point-like sources. The results are presented in Fig. 10. As shown by Fig. 10 (a), for J0206+4302u, the predicted SED at energies over  $\sim 100 \text{ TeV}$  is significantly lower than the KM2A result. There might be two reasons. The first reason is that the KM2A data used here are extracted from the fitted spectral parameters (Cao

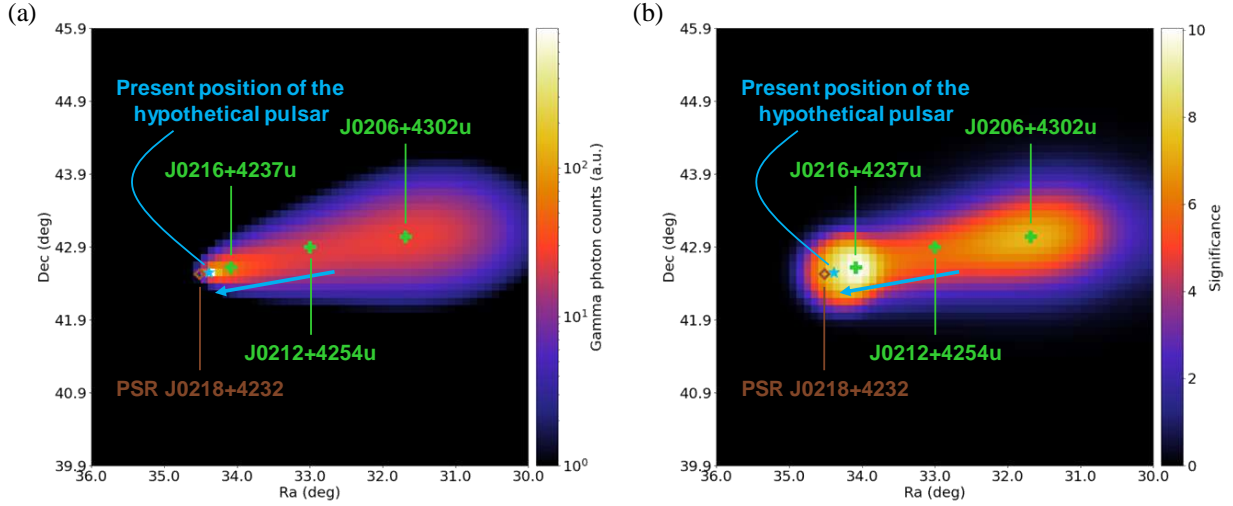


**Fig. 9.** The  $\gamma$  photon counts map without smooth and significance map at energies over 25 TeV based on the single traveling-PWN model. (a) The  $\gamma$  photon counts map calculated with  $D_0 = 4.8 \times 10^{24} \text{ cm}^2 \text{ s}^{-1}$ ,  $d = 0.375 \text{ kpc}$  and  $v = 1600 \text{ km s}^{-1}$ . The blue arrow indicates the proper-motion direction of the hypothetical pulsar in our model. (b) The predicted significance map seen from LHAASO. As a comparison, the LHAASO significance map on the dumbbell-like structure can be found at the left bottom of Figure 10 in the LHAASO catalog (Cao et al. 2024).

et al. 2024), which have error bars much smaller than that of the true experimental data. This can also explain the inconsistencies between the predicted SEDs of the other two sources and the corresponding KM2A results. We expect the up-to-date experimental data provided by the LHAASO collaboration in the future. The second reason is that, even the  $t_a$  is only about 14.6 kyr, it is not enough to avoid the cooling of electrons with energies of several hundreds TeV to PeV, which mainly contribute to the emission of  $> 100 \text{ TeV}$   $\gamma$  photons.

#### 4.2. Multiple traveling-PWNe modeling attempt

In the previous subsection, we discuss the scenario of using a single traveling-PWN to explain the LHAASO dumbbell-like structure. By applying some extreme parameters, like  $D_0$  of  $4.8 \times 10^{24} \text{ cm}^2 \text{ s}^{-1}$  and  $v$  of  $1600 \text{ km s}^{-1}$ , the predicted physical image have some similarities with the observed results of LHAASO-KM2A. However, the requirements for extreme parameters will significantly reduce the probability and reliability of this explanation. Moreover, there are some inconsistencies between the calculated  $\gamma$ -ray SEDs and fitted KM2A results. Thus, we prefer to use a traveling-PWN model contains multiple pulsars to explain the origin of the dumbbell-like structure.

As PSR J0218+4232 is the only know pulsar nearby and its position is close to the eastern LHAASO source J0216+4237u, we firstly assumed this pulsar as one of the traveling-PWNe in our model and expected the TeV halo generated by it can cover the eastern portion of the dumbbell-like structure. To check the feasibility of this hypothesis, we used the isotropic and homogeneous diffusion model in the previous subsection to simulate the TeV emission contribution of PSR J0218+4232. In the simulation, we assumed the diffusion coefficient around PSR J0218+4232 is similar to that around Geminga, which was a typical value within the one standard deviation interval of the statistical result on diffusion coefficients around 27 pulsars (Di Mauro et al. 2020). The spin-down luminosity and distance were set as  $2.4 \times 10^{35} \text{ erg s}^{-1}$  and 3.15 kpc, respectively (Cao et al. 2024). Based on the distance and the proper-motion in degree measured by the very long baseline interferometry (Du et al. 2014), the

proper-motion velocity was set as  $97.54 \text{ km s}^{-1}$ . The calculated  $\gamma$  photon counts map without smooth and significance map are presented in Fig. 11 (a)-(b). The positions of the three LHAASO sources and PSR J0218+4232 are pointed out on the figure. The magnetic field and radiation field model as well as the smooth method used in significance map calculation are the same with that in Subsection 4.1. Due to the long distance to earth and slow proper-motion velocity, there are no filaments left and only the electrons injected recently have contribution to  $\gamma$ -ray emission. Thus, under the isotropic and homogeneous diffusion condition, the expected TeV halo of PSR J0218+4232 can't even cover the exact spot of J0216+4237u.

The morphology of involving another traveling-PWN in the model is shown by Fig. 11 (c)-(d). The calculation was accomplished by adding an extra source term into the equation (8) and analytically solving the equation with the Green function method. The extra PWN was assumed to travel from (RA =  $34.3500^\circ$ , DEC =  $42.5763^\circ$ ) to (RA =  $31.6000^\circ$ , DEC =  $43.0500^\circ$ ) during the evolution. The parameters  $D_0$ ,  $d$  and  $v$  for the central pulsar were set as  $6.9 \times 10^{25} \text{ cm}^2 \text{ s}^{-1}$ , 0.375 kpc and  $800 \text{ km s}^{-1}$ , respectively. All the parameters applied here are no longer extreme parameters, but reasonable parameters for an ordinary pulsar. The  $v$  is relatively high but still acceptable. As presented by Fig. 11 (c)-(d), the TeV halo generated by an ordinary pulsar seems impossible to cover an almost  $3^\circ$  angle of expansion sky region, due to the cooling of UHE electrons (Zhang et al. 2021). Thus, the traveling-PWN model containing PSR J0218+4232 and an ordinary pulsar is still far from explaining the dumbbell-like structure.

According to the present results, the only known pulsar PSR J0218+4232 can be ruled out under the isotropic and homogeneous diffusion environment. However, this pulsar is still an important potential counterpart of the dumbbell-like structure in some other theories, like the asymmetric propagation of UHE electrons due to the turbulent magnetic field around the pulsar (Bao et al. 2024). As PSR J0218+4232 had been excluded, we attempted to use two relatively fast traveling-PWNe at short distance to explain the dumbbell-like structure. The first PWN was assumed to travel from (RA =  $34.3500^\circ$ , DEC =  $42.5763^\circ$ ) to

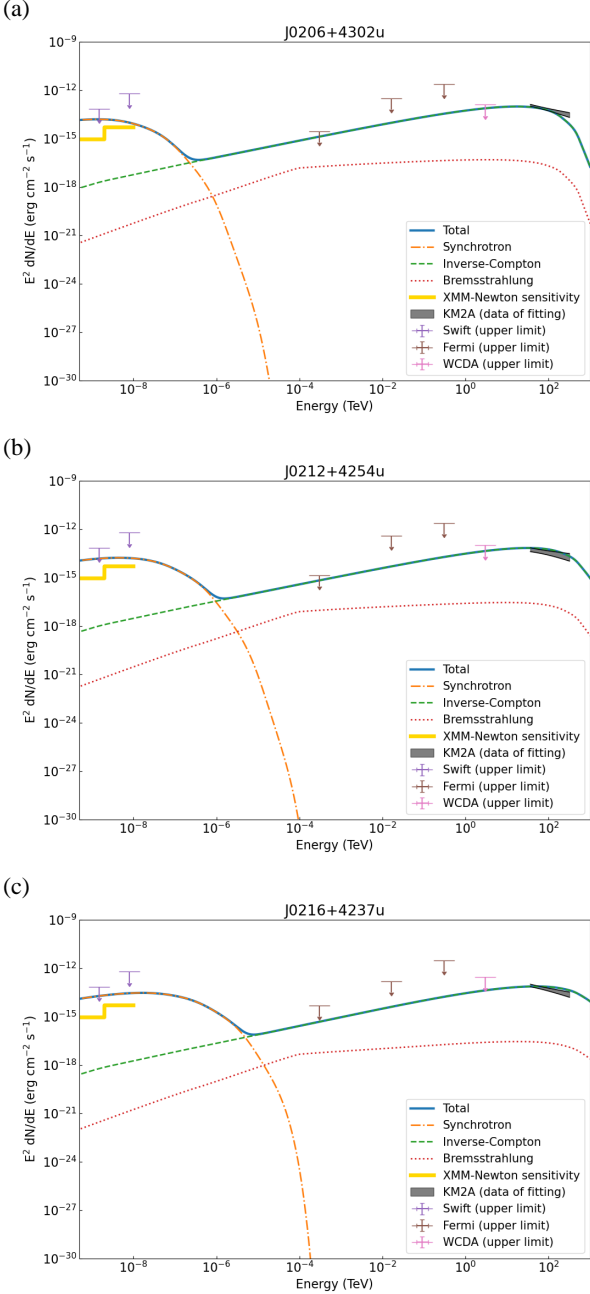


**Fig. 10.** The  $\gamma$ -ray SEDs calculated with the single traveling-PWN model, compared with fitted SEDs of KM2A and upper limits given by multi-wavelength and multi-messenger study. (a)-(c) Results of J0206+4302u, J0212+4254u and J0216+4237u, respectively.

(RA = 31.6000°, DEC = 43.0500°) during the evolution, while the second one was assumed to travel from (RA = 31.4500°, DEC = 43.2364°) to (RA = 34.2000°, DEC = 42.5300°). The major parameters of the two corresponding central pulsars are presented in Table 4. Due to the low TeV emission of PSR J0218+4232 predicted by the observation of Fermi-LAT and MAGIC (Acciari et al. 2021), we didn't consider the contribution of PSR J0218+4232 in this scenario. Fig. 11 (e)-(f) show the calculated  $\gamma$  photon counts map without smooth and significance map. Comparing with Fig. 11 (c)-(d), the morphology of the two hypothetical pulsars scenario is much more approximate to the LHAASO-KM2A result. For this scenario, both of the two > 25 TeV blobs are generated by the fresh PWN electrons injected re-

**Table 4.** Major parameters used for the double traveling-PWNe modeling attempt

The first pulsar			
Parameter	Value	Parameter	Value
$\dot{\xi}$ (erg s <sup>-1</sup> )	$3.25 \times 10^{34}$	$\eta$	$1.1 \times 10^{-6}$
$D_0$ (cm <sup>2</sup> s <sup>-1</sup> )	$6.9 \times 10^{25}$	$\delta$	0.33
$E_c$ (TeV)	500	$n$	2
$v$ (km s <sup>-1</sup> )	800	$\Gamma$	1.65
$d$ (kpc)	0.375	$\epsilon_{min}$	0.1
$t_a$ (kyr)	22.3	$\epsilon_{max}$	$1.0 \times 10^7$
The second pulsar			
Parameter	Value	Parameter	Value
$\dot{\xi}$ (erg s <sup>-1</sup> )	$3.25 \times 10^{34}$	$\eta$	$6.0 \times 10^{-7}$
$D_0$ (cm <sup>2</sup> s <sup>-1</sup> )	$6.9 \times 10^{25}$	$\delta$	0.33
$E_c$ (TeV)	400	$n$	2
$v$ (km s <sup>-1</sup> )	600	$\Gamma$	1.5
$d$ (kpc)	0.281	$\epsilon_{min}$	0.1
$t_a$ (kyr)	22.7	$\epsilon_{max}$	$1.0 \times 10^7$

cently and extended with the LHAASO PSF, while the entire extended structure is a combination of the diffused filaments left by the two PWNe. As all the parameters applied on the two pulsars were common values, the double traveling-PWNe explanation seems to be more applicable than the single traveling-PWN explanation. However, there are still some constraints on the characteristics of the two pulsars. According to Table 4, the conditions of short distance and fast traveling of the two pulsars need to be met simultaneously. Moreover, to form the dumbbell-like structure, the proper-motions of the two pulsars need to be opposite in direction, which will significantly reduced the occurring possibility of this scenario. The exact occurring possibility of different scenarios, including the single traveling-PWN and double traveling-PWNe explanation as well as the most ordinary explanation with the three LHAASO UHE sources corresponding to three PWNe (the leptonic modeling study of this explanation has been explored in Subsection 3.1), will be discussed in the next subsection.

#### 4.3. Occurring possibilities of different scenarios

As discussed in Subsection 4.1 and 4.2, to form a dumbbell-like structure as observed by KM2A with isotropic and homogeneous diffusion of PWN electrons, the corresponding central pulsars need to satisfy some requirements. Moreover, for the scenarios involving multiple pulsars, the spatial coincidence of pulsars is also essential. Thus, the occurring possibility  $P_k$  of each scenario can be calculated by

$$P_k = (P_{diff} P_d P_v)^k P_c. \quad (15)$$

Where  $k$  is the number of PWN.  $P_{diff}$ ,  $P_d$  and  $P_v$  describe the probability of the diffusion coefficient, distance and proper-motion velocity to meet the requirement, respectively.  $P_c$  denotes the probability of pulsars spatial coincidence by chance.

For the multiple traveling-PWNe explanation, there are no constraints on diffusion coefficient, which will result in  $P_{diff} = 1$ . For the single traveling-PWN explanation, an extremely low diffusion coefficient is required. As mentioned before, according to the statistical result on diffusion coefficients around 27 pulsars (Di Mauro et al. 2020), the diffusion coefficient required for the single traveling-PWN explanation is far out of the one standard deviation interval. Thus, the  $P_{diff}$  in this scenario is much lower

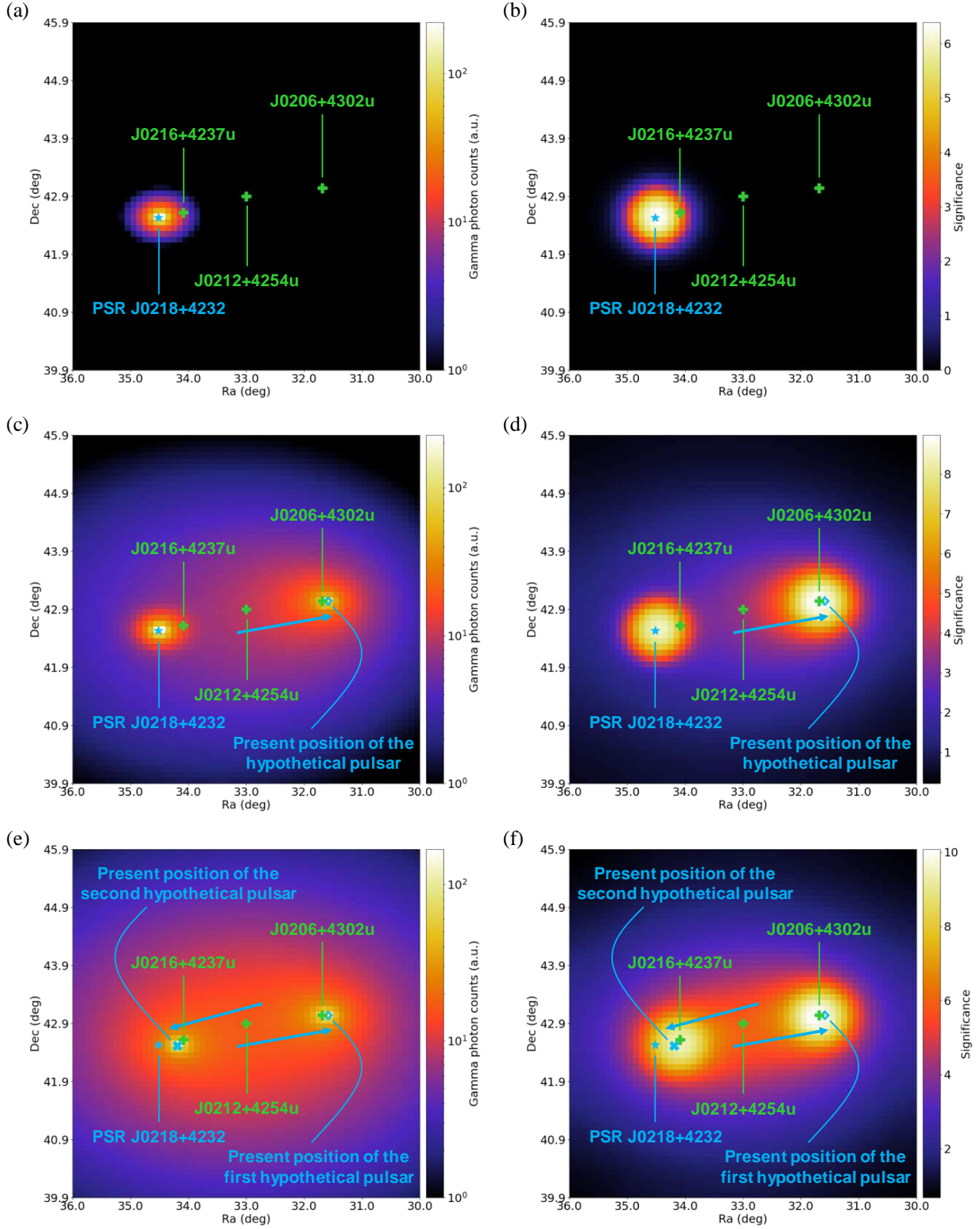


**Fig. 11.** The calculated  $\gamma$  photon counts map without smooth and significance map at energies over 25 TeV in multiple traveling-PWNe modeling attempt. (a)-(b) The  $\gamma$  photon counts map and significance map calculated with the model only containing PSR J0218+4232. (c)-(d) The  $\gamma$  photon counts map and significance map calculated with the model containing PSR J0218+4232 and another hypothetical pulsar. The blue arrow indicates the proper-motion direction of the hypothetical pulsar in our model. (e)-(f) The  $\gamma$  photon counts map and significance map calculated with the model containing two hypothetical pulsars. Here, the  $\gamma$ -ray emission from PSR J0218+4232 has been excluded.

than 0.32. No exact results can be provided here due to the lack of statistical samples.

The radial density profile of Galactic pulsars can be described by a gamma function (Lorimer et al. 2006)

$$\rho(R) = A \left( \frac{R}{R_\odot} \right)^F \exp \left[ -C \left( \frac{R - R_\odot}{R_\odot} \right) \right]. \quad (16)$$

**Table 5.** Occurring possibility of different scenarios

Scenario	$k$	$P_{\text{diff}}$	$P_d$	$P_v$	$P_c$	$P_k$
Single traveling-PWN explanation	1	$\ll 0.32$	0.0327	0.00013	1	$\ll 0.00014\%$
Double traveling-PWNe explanation	2	1	0.0327	0.1628	0.0273	0.00008%
Triple PWNe explanation	3	1	0.3495	1	0.0319	0.14%

Where  $R$  represents for the galactocentric radius.  $R_\odot = 8.3$  kpc is the distance between the Sun and Galactic center.  $A$ ,  $F$  and  $C$  are all fitting parameters depending on model. Along the direction perpendicular to the Galactic plane, the distribution of Galactic pulsars is assumed to satisfy a simple exponential function (Lorimer et al. 2006)

$$N(z) = D \exp\left(-\frac{|z|}{H}\right). \quad (17)$$

Here  $z$  denotes the height above the Galactic plane.  $D$  and  $H$  are also fitting parameters. Based on the fundamental geometrical relationship, it is not difficult to extract the distribution of  $d$  with equation (16) and (17). For the scenarios involving one pulsar or two pulsars, we assumed  $d < 0.5$  kpc. For the scenario involving three pulsars, according to Subsection 3.1,  $d$  was constrained to be lower than 4 kpc. Thus,  $P_d$  of the three scenarios containing one pulsar, two pulsars and three pulsars calculated by integrating the  $d$  distribution are 0.0327, 0.0327 and 0.3495, respectively. The fitting parameters used in the calculation follows the Model C fit in Lorimer et al. (2006).

Based on the statistical result on proper-motion velocities of 233 pulsars, the distribution of  $v$  is well described by a Maxwellian distribution (Hobbs et al. 2005) which can be written as

$$N(v) = \sqrt{\frac{2}{\pi}} \frac{v^2}{\sigma_v^3} \exp\left(-\frac{v^2}{2\sigma_v^2}\right). \quad (18)$$

Where the best-fit 1D root-mean-square (rms)  $\sigma_v$  is 265 km  $s^{-1}$ . In the most ordinary triple PWNe explanation, there was no need to set constraints on  $v$ . Thus,  $P_v$  of this scenario is 1. For the single-traveling PWN explanation, according to our exploration on the influence of  $v$ ,  $v$  was constrained to be higher than 1200 km  $s^{-1}$ . For the double traveling-PWNe explanation, we assumed  $v > 600$  km  $s^{-1}$ . Thus, based on equation (18),  $P_v$  of these two scenarios are 0.00013 and 0.1628, respectively.

At last, we considered the  $P_c$  in multiple traveling-PWNe explanation. The probability of two pulsars accidentally appear in the same sky region with position offset  $r_1$  can be expressed as (Mattox et al. 1997)

$$P(r_1) = 1 - \exp\left(-\frac{r_1^2}{r_0^2}\right), \quad (19)$$

where

$$r_0 = [\pi\rho(\xi)]^{-1/2}. \quad (20)$$

Here  $\rho(\xi)$  represents for the number density of local pulsars. Based on the method used in Cao et al. (2024), we examined the Australia Telescope National Facility (ATNF) pulsar catalog to check the number of pulsars within a  $20^\circ \times 5^\circ$  sky region centered on the exact spot of J0212+4254u. Considering the pulsar need to be energetic enough for being detected by LHAASO, a cut at  $\dot{\xi}/d^2 > 10^{34}$  erg  $s^{-1}$  kpc $^{-2}$  was applied during the examination, following Cao et al. (2024). As a result, before the cut on  $\dot{\xi}/d^2$ , there were 4 pulsars found within the  $20^\circ \times 5^\circ$  sky region,

while only 2 pulsars were left after the cut. The number density extracted from ATNF pulsar catalog is merely the number density of observed radio pulsars, which should be corrected into the actual number density of pulsars based on the beaming fraction multiplied by detection fraction (Johnston et al. 2020). Following Johnston et al. (2020), we assumed the final ratio between the number density of observed pulsars and the actual number density is 0.09. Thus, the  $\rho(\xi)$  around the dumbbell-like structure is  $\sim 765.36$  rad $^{-2}$ .

For the double traveling-PWNe explanation,  $P_c$  can be directly calculated by equation (19) and (20), based on the separation between the two hypothetical pulsars and  $\rho(\xi)$  of 765.36 rad $^{-2}$ . The result is 0.9814. However, since the two pulsars need to travel in almost opposite directions, this value should be multiplied by the probability of proper-motion directions coincidence by chance to acquire the actual  $P_c$ . According to our simulation, the appropriate angle between the proper-motion directions of the two pulsars to form the dumbbell-like structure is  $180 \pm 5^\circ$ . Thus, the actual  $P_c$  of this scenario is  $0.9814/36 = 0.0273$ .

The problem will be more complicated in the triple PWNe explanation. We firstly calculated the probability of accidentally having two pulsars located at the positions of J0206+4302u and J0216+4237u via equation (19) and (20). After that, the result was multiplied by the probability of having another pulsar coincidentally appeared in a  $0.2^\circ$  radius circle region (the radius was assumed to be the  $1\sigma$  value of LHAASO PSF) centered on the exact spot of J0212+4254u, which can be calculated by

$$P(S) = \rho(\xi)S \exp[-\rho(\xi)S]. \quad (21)$$

Here  $S$  is the area of the circle region in the unit rad $^2$ . At last, we could obtain the  $P_c$  of triple PWNe scenario as 0.0319.

As all the probabilities have been explored, based on equation (15),  $P_k$  of the three scenarios containing one pulsar, two pulsars and three pulsars are  $\ll 0.00014\%$ ,  $0.00008\%$  and  $0.14\%$ , respectively. As a brief summary, Table 5 presents all the parameters used in the calculation. It is worth noting that, even the ordinary triple PWNe explanation seems to have the highest complexity of model, the occurring possibility of this explanation is still much higher than that of the other two explanations. The reason is obvious. To explain the dumbbell-like structure consisting of three UHE sources with the proper-motion of one pulsar or two pulsars under the isotropic and homogeneous diffusion condition, many constraints on the characteristics of the pulsars are required, which can significantly increase the complexity of model and reduce the occurring possibility. Thus, it might not be a good choice to use the proper-motion of pulsar to explain a complicated extended structure in UHE band.

## 5. Conclusion and Discussion

The first LHAASO catalog presents six mysterious UHE sources only detected by LHAASO-KM2A (Cao et al. 2024). All of them are located far away from the Galactic plane and have no confirmed counterparts. Only two pulsars – PSR J0218+4232 and PSR J1740+1000 were found close to J0216+4237u and J1740+0948u. A more interesting thing is that J0206+4302u,



J0212+4254u and J0216+4237u are close in position and share a similar spectral shape. On the significance map, these three sources constitute a dumbbell-like structure.

To reveal the physical mechanisms hiding behind the six LHAASO UHE sources, especially the interesting dumbbell-like structure, we firstly conduct a multi-wavelength and multi-messenger study based on the Fermi-LAT, Swift-XRT, Planck, LAMBDA and IceCube neutrino datasets. As a result, only two  $\gamma$ -ray sources were observed by Fermi-LAT, which could be confirmed as the two known pulsars PSR J0218+4232 and PSR J1740+1000. For the X-ray band study based on Swift-XRT dataset, no abundant efficient photons were detected. According to the Planck and LAMBDA datasets, only the source J0007+5659u seemed to have a faint MC nearby. The potential hadronic origin of this source has been considered. Based on the HESE data release of 12 years and 10 years track-like events within the IceCube neutrino dataset, no neutrino event was found to be associated with the six sources. Moreover, with RATAN-600 radio telescope, the three sources constituted the dumbbell-like structure were observed at 3 to 5 epochs in February and April. No positive detection was found, and some of the preliminary results on upper limits were given: J0206+4302u ( $< 4$  mJy), J0218+4232 ( $< 6$  mJy) and J0212+4254u ( $< 6$  mJy). Since the present multi-wavelength and multi-messenger study can't give any confirmed counterparts, the origins of these six LHAASO sources remain elusive.

Based on the results of multi-wavelength and multi-messenger study, we performed leptonic and hadronic modeling study on the six LHAASO sources. In leptonic scenario, we assumed the six sources originated from Geminga-like PWNe whose injected electron spectra satisfy the simple power-law function with exponential cutoff. Our leptonic model indicates a very high exponential cutoff energy  $> 100$  TeV for all the six sources, which is common for pulsar injection (de Oña Wilhelmi et al. 2022). In hadronic scenario, we only study the p-p interaction of J0007+5659u, where the CRs are assumed to interact with the MC close to it. The same with leptonic scenario, a reasonable result was obtained. According to our modeling research, a worth noting thing is that the observation in X-ray band with sensitive telescopes like XMM-Newton can help to judge if J0007+5659u belong to leptonic or hadronic origin. Based on the best-fit parameters in hadronic modeling, we also calculated the expected neutrino flux from J0007+5659u. The result is more than one order of magnitude lower than the 10 years observation sensitivity of IceCube-Gen2. However, there still remains the possibility of detecting associated neutrinos with some other proposed next generation neutrino observatories like TRIDENT (Ye et al. 2022) and NEON (Zhang et al. 2023).

For the dumbbell-like structure we are most interested in, which is also recognized as three point-like sources in the LHAASO catalog (Cao et al. 2024), a traveling PWN model under isotropic and homogeneous diffusion condition was studied. We firstly explored the scenario containing only one traveling-PWN. The impact of diffusion coefficient, distance and proper-motion velocity on the final morphology of  $\gamma$ -ray halo was discussed. As a result, we found that to generate a dumbbell-like structure, the diffusion coefficient had to be more than an order of magnitude lower than the typical value around Geminga, while the proper-motion velocity needed to be faster than  $1200 \text{ km s}^{-1}$ . Moreover, the distance within a proper range was also essential. With all these requirements satisfied and adapting a typical PWN spin-down evolution history following Ding et al. (2021), we could obtain a significance map accord with the result of KM2A. However, the extreme parameters required and the in-

consistencies in spectral shape make this explanation seem to be incredible. As the single traveling-PWN model had difficulties in explaining the dumbbell-like structure, we also studied the model containing two traveling-PWNe. The only known pulsar PSR J0218+4232 is involved in the study at first, and has been ruled out due to its long distance to earth and slow proper-motion velocity. This pulsar is still an important potential counterpart based on some other theories. Assuming two hypothetical pulsars with relatively short distance and fast proper-motion velocity, the double traveling-PWNe model can also generate an extended structure approximate to the dumbbell-like structure observed by KM2A. Since no extreme parameters were applied, we thought this explanation is more applicable to explain the dumbbell-like structure, comparing with the single traveling-PWN scenario. The exact occurring possibility of these two explanations and the most ordinary explanation with the three LHAASO UHE sources corresponding to three PWNe, as discussed in Subsection 3.1, were also calculated. As a result, the occurring possibility of the ordinary triple PWNe explanation is about three orders of magnitude higher than that of the explanations requiring less PWNe. It is obvious that the constraints on the characteristics of the corresponding central pulsars can significantly increase the complexity of model and reduce the occurring possibility, even for the double traveling-PWNe scenario. Thus, it seems unreasonable to use the proper-motion of pulsar to explain a complicated extended structure in UHE band. As the ordinary triple PWNe explanation has the highest occurring possibility, we expected the XMM-Newton observation in X-ray band and Five-hundred-meter Aperture Spherical radio Telescope (FAST) observation in radio band on the exact spot of J0206+4302u, J0212+4254u and J0216+4237u can reveal the origin of the dumbbell-like structure. Also, the up-to-date experimental data provided by the LHAASO collaboration in the future is expected.

*Acknowledgements.* The authors thank Shaoqiang Xi, Ruoyu Liu, Sujie Lin, Renfeng Xu, Wenjun Huang and Sheng Tang for the helpful discussion. We thank Timur Mufakharov and Yulia Sotnikova for the RATAN-600 observation. This work was supported by the National Natural Science Foundation of China (NSFC) Grants No. 12261141691 and No. 12005313. We thank the support from Fundamental Research Funds for the Central Universities, Sun Yat-sen University, No. 24qnpy123.

## Appendix A: Multi-wavelength and multi-messenger data analysis

### Appendix A.1: Fermi-LAT data analysis

The Fermi-LAT data is publicly available on the Fermi-LAT website<sup>9</sup> and can be analyzed with the **Fermitools** developed by the Fermi-LAT collaboration. After acquiring the Fermi-LAT data of 10 years observation, we used the **gtselect** function to filter the  $\gamma$  photons outside the ROI centered on the source to be studied. The radius of ROI was chosen to be  $1.5^\circ$  for  $\gamma$ -ray fluxes calculation and  $5^\circ$  for TS maps calculation. The  $\gamma$  photons were also selected by their energies. Only the  $\gamma$  photons with energy between 300 MeV and 300 GeV were involved in the analysis. The background contribution was subtracted by including the Galactic diffuse model (gll\_iem\_v07) and the isotropic background (iso\_P8R3\_SOURCE\_V3\_v1), as well as the 4FGL catalog.

The  $\gamma$ -ray fluxes of the six LHAASO UHE sources were obtained via a binned maximum-likelihood analysis. The recommended power-law spectral models (Cao et al. 2024; Tam et al. 2020) for each source were added into the input model files generated by **LATSourceModel** Python package, as shown below

$$\frac{dN}{dE} = N_0 \left( \frac{E}{E_0} \right)^{-\alpha_0}. \quad (\text{A.1})$$

The normalization  $N_0$  and spectral index  $\alpha_0$  were allowed to change, while the reference energy  $E_0$  was fixed. After running the maximum-likelihood analysis function **gtlike**, the  $\gamma$ -ray fluxes in MeV - GeV band could be acquired. Due to the lack of observation data, the results had error bars larger than truth-values. Thus, we also calculated the SED upper limits with **UpperLimits**, a Python package of **Fermitools**, to set constraints on our leptonic and hadronic models.

After the binned maximum-likelihood analysis, the TS maps of the six LHAASO sources were calculated by running **gttsmap** function. The input model files used in this step were the fitted model files as the outputs of the maximum-likelihood analysis with some modifications. All the free parameters in these model files were set fixed, and for calculating TS maps containing 4FGL sources close to the LHAASO sources with position offset lower than  $0.5^\circ$ , the corresponding 4FGL source models were removed.

### Appendix A.2: Swift-XRT data analysis

We checked the Swift-XRT dataset and only found the source J0206+4302u had X-ray data within the  $0.3^\circ$  ROI centered on it. No accurate energy spectrum could be extracted from these data due to the lack of efficient photons. However, the photon flux upper limit could be calculated via the X-ray image analysis package **XIMAGE** integrated in **HEASOFT** software<sup>10</sup>, whose value was  $1.55 \times 10^{-2} \text{ s}^{-1}$ . Based on the photon flux upper limit and the photo-electric absorption model describing the photon flux attenuation during the transmitting process, the upper limit of SED can be obtained. Here, the effect of photo-electric absorption was considered to meet an exponential damping function as shown below

$$M(E) = \exp[-N_{\text{H}}\sigma_{\text{pe}}(E)]. \quad (\text{A.2})$$

<sup>9</sup> <https://fermi.gsfc.nasa.gov/cgi-bin/ssc/LAT/LATDataQuery.cgi>

<sup>10</sup> The software can be downloaded from <https://heasarc.gsfc.nasa.gov/lheasoft/download.html>

Where  $N_{\text{H}}$  is the column density of hydrogen. It was set to the Galactic value at the sky region around J0206+4302u<sup>11</sup>, which equals to  $9.84 \times 10^{20} \text{ cm}^{-2}$ .  $\sigma_{\text{pe}}(E)$  is the photo-electric cross-section.

Similar to the analysis of Fermi-LAT data, a power-law model was used to describe the original energy spectrum of X-ray without considering photo-electric absorption. Since no accurate spectral shape could be acquired with the limited efficient photons, the spectral index was assumed to be 1.8 (Giommi et al. 2021). By integrating the product of the power-law spectrum and equation (A.2), and comparing with the photon flux upper limit calculated before, the upper limit of normalization were obtained. Then, the upper limit of SED could be worked out based on this upper limit. Assuming the other five LHAASO sources had X-ray photon fluxes similar to or lower than that of J0206+4302u, since there were no observation data, we applied the SED upper limit of J0206+4302u to all of them.

## Appendix B: Expected neutrino flux calculation

The production rate and spectrum of neutrinos from p-p interaction relies on the type of meson decay and the flavor of generated neutrinos. For muonic neutrinos, the neutrino flux per unit of energy can be calculated via the equation below (Kelner et al. 2006; De Sarkar & Gupta 2022)

$$\Phi_{\nu}(E_{\nu}) = \frac{cn_{\text{MC}}}{4\pi d^2} \int \frac{1}{x} \sigma_{\text{pp}}(E_{\nu}/x) J_p(E_{\nu}/x) F_{\nu}(x, E_{\nu}/x) dx. \quad (\text{B.1})$$

Where  $x = E_{\nu}/E_p$  denotes the variable of integration.  $n_{\text{MC}}$  is the number density of the MC in p-p interaction.  $E_{\nu}$  and  $E_p$  are the energies of produced neutrinos and injected protons, respectively.  $\sigma_{\text{pp}}(E_{\nu}/x)$  stands for the inelastic cross-section of p-p interaction, which is given by a fitting formula (Kelner et al. 2006; De Sarkar & Gupta 2022)

$$\sigma_{\text{pp}}(E_p) = 34.3 + 1.88L + 0.25L^2. \quad (\text{B.2})$$

In equation (B.2), the cross-section is presented in the unit mb (mbarn).  $L = \ln(E_p/1 \text{ TeV})$  is a dimensionless variable related to  $E_p$ .  $J_p(E_{\nu}/x)$  denotes the energy distribution of protons as shown in equation (3) of the main text.  $F_{\nu}(x, E_{\nu}/x)$  describes the energy spectra of neutrinos produced through meson decay. For muonic neutrinos generated from the decays of charged pions and secondary muons,  $F_{\nu}(x, E_{\nu}/x)$  have different forms (Kelner et al. 2006). The lower and upper limits of integration are also decided by the type of meson decay. In pion decay scenario, since the  $F_{\nu}(x, E_{\nu}/x)$  has a sharp cutoff at  $x = 0.427$  (Kelner et al. 2006), the upper limit of integration can be simply set as 0.427. And in muon decay scenario, the integration should be conducted with  $x$  varying from 0 to 1.

Based on equation (B.1) and (B.2), we calculated the expected muonic neutrino flux from J0007+5659u with the best-fit parameters in our hadronic model as presented in Subsection 3.2 of the main text, and compared with 10 years observation sensitivity of IceCube-Gen2 (Aartsen et al. 2019). Fig. B.1 shows the result. The fluxes of other flavour neutrinos are expected to be the same as that of muonic neutrino, as  $\nu_e : \nu_{\mu} : \nu_{\tau} = 1 : 1 : 1$  at Earth. As shown in Fig. B.1, the calculated neutrino SED of J0007+5659u is much lower than the sensitivity limit of IceCube-Gen2 with energy ranging from 1 TeV to 1 PeV.

<sup>11</sup> The Galactic value of column density of hydrogen can be checked on <https://www.swift.ac.uk/analysis/nhtot/>

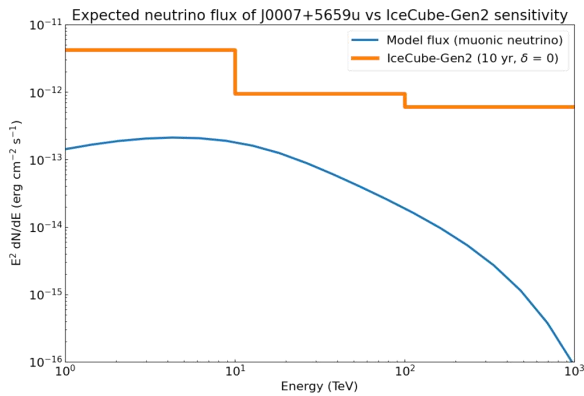


**Fig. B.1.** The expected muonic neutrino flux generated by p-p interaction for J0007+5659u, comparing with 10 years observation sensitivity of IceCube-Gen2 (Aartsen et al. 2019).

Moreover, the neutrino flux from  $\gamma$ -p interaction (Hümmer et al. 2010) for the six LHAASO UHE sources was also considered. We assumed the interactions happening among the  $\gamma$  photons emitted by the six sources and Galactic CR protons. Since the  $\gamma$ -ray fluxes of the six sources are too weak, the expected neutrino flux in  $\gamma$ -p interaction calculated with Galactic CR proton spectrum (collaboration et al. 2019) is much lower than that in p-p interaction.

## References

Aartsen, M., Ackermann, M., Adams, J., et al. 2019, arXiv preprint arXiv:1911.02561

Aartsen, M. G., Abbasi, R., Abdou, Y., et al. 2013, Physical review letters, 111, 021103

Aartsen, M. G., Ackermann, M., Adams, J., et al. 2017, Journal of Instrumentation, 12, P03012

Aartsen, M. G. et al. 2018a, Science, 361, eaat1378

Aartsen, M. G. et al. 2018b, Science, 361, 147

Aartsen, M. G. et al. 2020, Phys. Rev. Lett., 124, 051103

Abbasi, R., Ackermann, M., Adams, J., et al. 2023a, Updated directions of IceCube HESE events with the latest ice model using DirectFit, Tech. rep.

Abbasi, R. et al. 2021 [arXiv:2101.09836]

Abbasi, R. et al. 2022, Science, 378, 538

Abbasi, R. et al. 2023b, Science, 380, adc9818

Abbasi, R. et al. 2023c, Astrophys. J. Lett., 945, L8

Abdo, A., Ackermann, M., Ajello, M., et al. 2009, The Astrophysical Journal, 707, 1310

Abdollahi, S., Acero, F., Ackermann, M., et al. 2020, The Astrophysical Journal Supplement Series, 247, 33

Abeyskara, A., Albert, A., Alfaro, R., et al. 2017, Science, 358, 911

Acciari, V. A., Ansoldi, S., Antonelli, L. A., et al. 2021, The Astrophysical Journal, 922, 251

Bao, Y., Liu, R.-Y., Giacinti, G., Zhang, H.-M., & Chen, Y. 2024, arXiv preprint arXiv:2407.02829

Bolatto, A. D., Wolfire, M., & Leroy, A. K. 2013, Annual Review of Astronomy and Astrophysics, 51, 207

Burrows, D. N., Hill, J., Nousek, J., et al. 2005, Space science reviews, 120, 165

Cao, Z., Aharonian, F., An, Q., et al. 2024, The Astrophysical Journal Supplement Series, 271, 25

collaboration, D., An, Q., Asfandiyarov, R., et al. 2019, Science advances, 5, eaax3793

Collaboration\*, I. 2013, Science, 342, 1242856

Dame, T. & Thaddeus, P. 2022, The Astrophysical Journal Supplement Series, 262, 5

de Oña Wilhelmi, E., López-Coto, R., Amato, E., & Aharonian, F. 2022, The Astrophysical Journal Letters, 930, L2

De Sarkar, A. & Gupta, N. 2022, The Astrophysical Journal, 934, 118

Delahaye, T., Lavalley, J., Lineros, R., Donato, F., & Fornengo, N. 2010, Astronomy & Astrophysics, 524, A51

Delahaye, T., Lineros, R., Donato, F., Fornengo, N., & Salati, P. 2008, Physical Review D, 77, 063527

Di Mauro, M., Manconi, S., & Donato, F. 2020, Physical Review D, 101, 103035

Di Sciascio, G., Collaboration, L., et al. 2016, Nuclear and particle physics proceedings, 279, 166

Ding, Y.-C., Li, N., Wei, C.-C., Wu, Y.-L., & Zhou, Y.-F. 2021, Physical Review D, 103, 115010

Du, Y., Yang, J., Campbell, R. M., et al. 2014, The Astrophysical Journal Letters, 782, L38

Fang, K. & Bi, X.-J. 2022, Physical Review D, 105, 103007

Fang, K., Bi, X.-J., Yin, P.-F., & Yuan, Q. 2018, The Astrophysical Journal, 863, 30

Fang, K. & Halzen, F. 2024, JHEAp, 43, 140

Funk, S., Hinton, J., Consortium, C., et al. 2013, Astroparticle Physics, 43, 348

Gaensler, B. M. & Slane, P. O. 2006, Annu. Rev. Astron. Astrophys., 44, 17

Geyer, C. J. 1992, Statistical science, 473

Giommi, P., Perri, M., Capalbi, M., et al. 2021, Monthly Notices of the Royal Astronomical Society, 507, 5690

Hahn, J. 2015, in The 34th International Cosmic Ray Conference

Hobbs, G., Lorimer, D., Lyne, A., & Kramer, M. 2005, Monthly Notices of the Royal Astronomical Society, 360, 974

Hou, B., Wu, S., & Chen, S. 2024, arXiv preprint arXiv:2405.11826

Hümmer, S., Rügger, M., Spanier, F., & Winter, W. 2010, The Astrophysical Journal, 721, 630

Hussein, M. & Shalchi, A. 2014, The Astrophysical Journal, 785, 31

Jacob, J. C., Katz, D. S., Berriman, G. B., et al. 2009, International Journal of Computational Science and Engineering, 4, 73

Jansson, R. & Farrar, G. R. 2012, The Astrophysical Journal, 757, 14

Johnston, S., Smith, D., Karastergiou, A., & Kramer, M. 2020, Monthly Notices of the Royal Astronomical Society, 497, 1957

Kelner, S. R., Aharonian, F. A., & Bugayov, V. V. 2006, Physical Review D, 74, 034018

Li, W., Huang, T.-Q., Xu, D., & He, H. 2024, Astrophys. J., 969, 6

Lorimer, D. R., Faulkner, A., Lyne, A., et al. 2006, Monthly Notices of the Royal Astronomical Society, 372, 777

Mattox, J., Schachter, J., Molnar, L., Hartman, R., & Patnaik, A. 1997, The Astrophysical Journal, 481, 95

Nakar, E., Ando, S., et al. 2009, The Astrophysical Journal, 703, 675

Neronov, A. & Semikoz, D. 2020, Physical Review D, 102, 043025

Popescu, C., Yang, R., Tuffs, R., et al. 2017, Monthly Notices of the Royal Astronomical Society, 470, 2539

Reid, M., Dame, T., Menten, K., & Brunthaler, A. 2016, The Astrophysical Journal, 823, 77

Reid, M., Menten, K., Brunthaler, A., et al. 2019, The Astrophysical Journal, 885, 131

Shalchi, A. 2009, Astroparticle Physics, 31, 237

Su, Y., Yang, J., Zhang, S., et al. 2019, The Astrophysical Journal Supplement Series, 240, 9

Tam, P.-H. T., Lee, K., Cui, Y., et al. 2020, The Astrophysical Journal, 899, 75

Tauber, J. A., Mandolesi, N., Puget, J.-L., et al. 2010, Astronomy & Astrophysics, 520, A1

Ye, Z., Hu, F., Tian, W., et al. 2022, arXiv preprint arXiv:2207.04519

Yoast-Hull, T. M., Gallagher, J. S., & Zweibel, E. G. 2016, Monthly Notices of the Royal Astronomical Society: Letters, 457, L29

Zhang, H., Cui, Y., Dong, P., et al. 2023

Zhang, Y., Liu, R.-Y., Chen, S., & Wang, X.-Y. 2021, The Astrophysical Journal, 922, 130